

COMPUTATIONAL FLUID DYNAMIC ANALYSIS OF  
THE PURIFICATION PROCESS OF THE  
NEUTRINO DETECTOR KAMLAND

by

AARON MITCHELL COSSEY

A THESIS

Submitted in partial fulfillment of the requirements  
for the degree of Master of Sciences in the  
Department of Mechanical Engineering  
in the Graduate School of  
The University of Alabama

TUSCALOOSA, ALABAMA

2009

Copyright Aaron Mitchell Cossey 2009  
ALL RIGHTS RESERVED

## ABSTRACT

A simplified two-dimensional finite volume axisymmetric mesh was constructed that represented the geometry of the Kamioka Liquid scintillator Anti-Neutrino Detector (KamLAND) experiment in order to perform a computational fluid dynamics (CFD) analysis of the purification process of the liquid scintillator (LS). 1,000 tons of the LS, contained within a 13 meter-diameter spherical balloon in the center of the detector, is purified in a continuous process where the LS is simultaneously withdrawn from the bottom and replaced at the top of the detector. During this purification process, the interface between the newly purified and unpurified LS is not stratified horizontally as expected, but instead mixing is observed, reducing the efficiency of the process and preventing the desired level of purification throughout the LS.

Using the commercial CFD software FLUENT, the purification process of the experiment was simulated based on the conditions and data previously recorded during the purification phase. The CFD analysis of the experiment was modeled as a transient problem, with flow and heat transfer solved. The phenomenon of natural convection was modeled using the Boussinesq approximation. The volume of fraction (VOF) method was used to track the interaction between the purified and unpurified liquids in the simulation.

The CFD simulation will be used to test proposed improvements to the purification process for future purification programs of KamLAND. The CFD simulation will serve as a guide to test these improvements and improve the efficiency of the process.

## DEDICATION

I would like to dedicate this thesis to all of my friends and family who provided me with their support to the very end. Without their support, I do not know if I would have ever been able to finish this thesis.

## ACKNOWLEDGMENTS

I would like to thank all of my colleagues, friends, and faculty members who have helped me with this project. In particular, I would like to thank my supervisor Dr. Keith Woodbury for his support and patience, even when I did not think that I would ever finish. His knowledge and suggestions for my CFD simulation were of great benefit to me. I would like to thank the Physics Department of the University of Alabama's members of the KamLAND Collaboration, Dr. Andreas Piepke and Greg Keefer, for the opportunity to work on this project.

I would also like to thank Dr. Michael Freeman and Dr. Will Schreiber for serving on my thesis committee and providing their recommendations.

## LIST OF ABBREVIATIONS AND SYMBOLS

BO	buffer oil of detector
mBq	milli-Bequerel, decay / 1,000 second
CAD	Computer Aided Drawing
CFD	Computational Fluid Dynamics
$\rho$	density, kg / m <sup>3</sup>
$\bar{\nu}_e$	electron anti-neutrino
$g$	gravitational constant, 9.81 m/s <sup>2</sup>
ID	inner detector
KamLAND	Kamioka Liquid scintillator Anti-Neutrino Detector
K	Kelvin degree
$k$	thermal conductivity
LS	liquid scintillator of detector
$\dot{m}$	mass transfer rate
m	meter
$\mu\text{m}$	micrometer or 10 <sup>-6</sup> meter
mm	millimeter or 10 <sup>-3</sup> meter
OD	outer detector
PMTs	photomultiplier tubes
$r$	dimensional radial coordinate
$S_h$	volumetric heat rate, W / m <sup>3</sup>

UDF	user defined function
$v_x$	dimensional axial velocity
$v_r$	dimensional radial velocity
$v_z$	swirl velocity
$\nu$	kinematic viscosity
VOF	volume of fluid
$x$	dimensional axial coordinate

## CONTENTS

ABSTRACT .....	ii
DEDICATION .....	iii
ACKNOWLEDGMENTS .....	iv
LIST OF ABBREVIATIONS AND SYMBOLS .....	v
LIST OF TABLES .....	x
LIST OF FIGURES .....	xi
CHAPTER 1 INTRODUCTION.....	1
1.1 A Brief Description of KamLAND.....	1
1.2 The Detector of KamLAND .....	2
1.3 Purification System of the Detector .....	4
1.4 Objective of Project .....	8
1.5 Scope of Project .....	8
CHAPTER 2 CFD PHYSICAL MODELS .....	10
2.1 CFD Introduction .....	10
2.2 Governing Equations .....	11
2.2.1 Assumptions to Simply the CFD Simulation.....	12
2.2.2 The Mass Conservation and Momentum Equations .....	12

2.2.3 The Energy Equation and Heat Transfer Theory .....	14
2.2.4 Natural Convection and the Boussinesq Model.....	15
2.2.5 Volume of Fluid (VOF) Theory.....	17
<b>CHAPTER 3 CFD KAMLAND MODEL .....</b>	<b>19</b>
3.1 Steps in Solving CFD Problem.....	19
3.2 The Modeling Goals .....	19
3.3 Creating the Model Geometry .....	20
3.3.1 Simplyfying the KamLAND Geometry.....	22
3.3.2 Meshing the KamLAND Geometry.....	23
3.3.3 Description of the Grid .....	28
3.4 Pre-Processing of FLUENT .....	29
3.4.1 Reading in the Grid.....	29
3.4.2 Defining the Material Properties and Boundary Conditions.....	29
3.4.3 Enabling the Desired Physical Models .....	33
3.4.5 Initializing the Solution.....	34
3.4.6 Selecting the Solution Controls .....	36
3.5 Computing the Solution of FLUENT .....	40
3.6 Post-Processing the Results of FLUENT.....	42

CHAPTER 4	RESULTS AND DISCUSSION .....	43
CHAPTER 5	CONCLUSIONS.....	52
REFERENCES	.....	55
APPENDIX A	KAMLAND COLLABORATION.....	A-1
APPENDIX B	METHOD OF TRACKING $^{222}\text{Rn}$ DAUGHTERS.....	B-1
APPENDIX C	MATERIALS PARAMETERS.....	C-1
APPENDIX D	BOUNDARY CONDITIONS .....	D-1
APPENDIX E	USER DEFINED FUNCTION TEMPERATURE PROFILE .....	E-1
APPENDIX F	KAMLAND CFD WORK SHEET .....	F-1

LIST OF TABLES

*Table 1-1.* Background activities in KamLAND before and after purification. .... 6

*Table 3-1.* Details of the CFD mesh created in GAMBIT..... 28

*Table F-1.* KamLAND\_2Dv10 Work Sheet..... F-1

## LIST OF FIGURES

<i>Figure 1-1.</i> An illustration of the KamLAND hall and access tunnels. ....	3
<i>Figure 1-2.</i> Conceptual drawing of KamLAND. ....	4
<i>Figure 1-3.</i> Purified LS volume and flow rate over 1st purification campaign. ....	5
<i>Figure 1-4.</i> Distinct separation of old and new LS during first purification phase. ....	7
<i>Figure 3-1.</i> KamLAND detailed schematic. ....	20
<i>Figure 3-2.</i> KamLAND geometry created using Pro/E. ....	21
<i>Figure 3-3.</i> GAMBIT geometry created from IGES file. ....	22
<i>Figure 3-4.</i> GAMBIT simplified geometry. ....	23
<i>Figure 3-5.</i> Simple geometry of model used to test the grid resolution required. ....	25
<i>Figure 3-6.</i> Mesh used in KamLAND CFD simulation. ....	25
<i>Figure 3-7.</i> Enlarged view of the boundary layer used on the walls of the LS domain. ....	26
<i>Figure 3-8.</i> Enlarged view of skewed cells in outlet pipe. ....	27
<i>Figure 3-9.</i> Density and mass flow rate of LS over the course of the first purification process. .	30
<i>Figure 3-10.</i> Plots of temperature versus time of four elevation levels within the OD. ....	31
<i>Figure 3-11.</i> Polynomial trendline of OD temperature versus distance along z-axis. ....	32
<i>Figure 3-12.</i> Measured temperature (°C) distribution in KamLAND. ....	35
<i>Figure 3-13.</i> Initial temperature distribution calculated by FLUENT. ....	35
<i>Figure 3-14.</i> Temperature distribution of solution with only the energy equation solved. ....	37
<i>Figure 3-15.</i> Temperature distribution with energy and flow equations coupled. ....	37
<i>Figure 3-16.</i> Temperature distribution in simple CFD model with only energy solved. ....	38

<i>Figure 3-17.</i> Temperature distribution in simple CFD model with energy and flow solved. ....	39
<i>Figure 3-18.</i> KamLAND geometry partitioned for parallel computing. ....	40
<i>Figure 3-19.</i> Scaled residuals plot of the KamLAND CFD simulation. ....	41
<i>Figure 4-1.</i> Montage of KamLAND after one day of purification. ....	44
<i>Figure 4-2.</i> Montage of KamLAND after one week of purification. ....	44
<i>Figure 4-3.</i> Montage of KamLAND after two weeks of purification. ....	45
<i>Figure 4-4.</i> Montage of KamLAND after three weeks of purification. ....	45
<i>Figure 4-5.</i> Montage of KamLAND after four weeks of purification. ....	46
<i>Figure 4-6.</i> Montage of KamLAND after five weeks of purification. ....	46
<i>Figure 4-7.</i> Montage of KamLAND after six weeks of purification. ....	47
<i>Figure 4-8.</i> Montage of KamLAND after seven weeks of purification. ....	47
<i>Figure 4-9.</i> Montage of KamLAND after eight weeks of purification. ....	48
<i>Figure 4-10.</i> Montage of KamLAND after nine weeks of purification. ....	48
<i>Figure 4-11.</i> Montage of KamLAND CFD simulation temperature profile. ....	49
<i>Figure 4-12.</i> Spacial distribution of BiPo events with the fiducial volume cut removed. ....	51
<i>Figure B-1.</i> Decay scheme for $^{222}\text{Rn}$ . ....	B-2
<i>Figure B-2.</i> Pairs of events that satisfy energy selection cut for $^{214}\text{Bi}$ - $^{214}\text{Po}$ events. ....	B-3
<i>Figure B-3.</i> Dots representing $^{214}\text{Bi}$ - $^{214}\text{Po}$ event pair from the decay of $^{222}\text{Rn}$ in the detector. .	B-4

## CHAPTER 1 INTRODUCTION

### 1.1 A Brief Description of KamLAND

The Kamioka Liquid scintillator Anti-Neutrino Detector (KamLAND) is an experiment at the Kamioka Observatory, an underground neutrino observatory near Toyama, Japan, that was built to detect electron anti-neutrinos ( $\bar{\nu}_e$ ) (KamLAND Wiki). The group of international scientists, professors, and students from the United States (including the Physics Department of the University of Alabama), Japan, and Europe working on the experiment is known as the KamLAND Collaboration and is listed in Appendix A. The KamLAND Collaboration has reported that the experiment has determined the associated oscillation parameter  $\Delta m^2_{21}$  to unprecedented precision, has helped constrain the neutrino mixing angle  $\theta_{12}$ , and has explored the potential application of neutrinos as a geophysical probe. The detector is currently undergoing an upgrade to the purification process which will enable KamLAND to execute a low energy solar neutrino program to detect  $^7\text{Be}$  solar neutrinos in parallel with this already highly fruitful anti-neutrino program (KamLAND Collaboration).

The KamLAND project was proposed in 1994. In 1997, the full budget was funded by the Japanese Ministry of Education. In 1999 the United States Department of Energy approved the US-KamLAND proposal. Following a five year period for construction of the detector and the underground facility, KamLAND was launched into data-taking on January 22, 2002. The main objectives of KamLAND are to aim at studying reactor electron anti-neutrino oscillations with more than 100 kilometer baseline, simultaneously searching for neutrinos from both

terrestrial and solar sources. Data taking has been consistently gathered since March 2002 (Suzuki et al., 2005).

During the summer of 2007, the first upgraded purification process of the liquid scintillator (LS) used in the detection of the solar neutrinos encountered difficulties in attaining the desired reduction of the levels of the radioactive impurities that interferes with low level energy detection. During the purification process, the liquid scintillator is purified in a continuous process where LS is simultaneously withdrawn from the bottom and replaced at the top of the detector. The interface between the newly purified and unpurified LS was not stratified horizontally as expected due to unaccounted for mixing inside of the detector. This mixing reduced the efficiency of the process and prevented the desired level of purification throughout the LS. There is no understanding of how the flow field present during the purification process affects this mixing.

## 1.2 The Detector of KamLAND

The detector was built in the Kamioka mine, 1,000 meters under the top of Mt. Ikenoyama, which was the site of the old Kamiokande: the 3000 cubic meter water Cerenkov detector which played a leading role in the study of neutrinos produced via cosmic rays and also helped to pioneer the subject of neutrino astronomy. After dismantling the Kamiokande detector, the rock cavity was enlarged to be 20 meters in diameter and 20 meters in height. An illustration of the detector within the mine is displayed in Figure 1-1. Background events for the neutrino detection are caused by undesired radioactive particles which come into the scintillator from the outside or inside of the detector. To guard against external radiation, the detector consists of a cylinder containing a series of concentric spherical shells. KamLAND consists of three distinct regions: the inner detector, the buffer region, and the outer detector. The inner

neutrino detector is 1000 tons of ultra pure liquid scintillator (LS) located at the center of the detector. The KamLAND LS is a chemical cocktail of 80% dodecane, 20% 1,2,4-trimethylbenzene, and 1.52 g/liter 2,5-diphenyloxazole as a fluor.

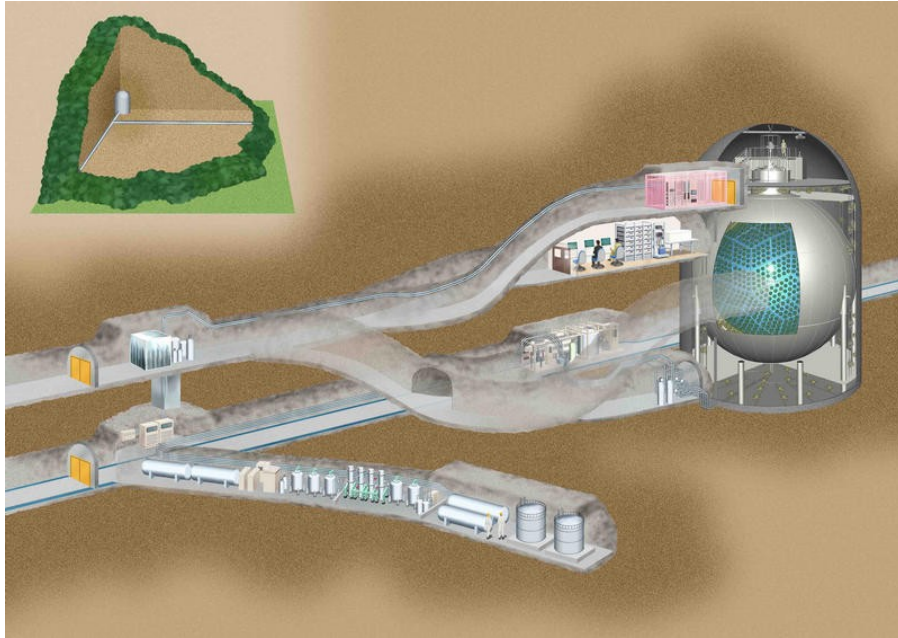


*Figure 1-1.* An illustration of the KamLAND hall and access tunnels.

The scintillator is housed in a 13 meter-diameter spherical balloon made of 2 layers of nylon with a total thickness of 135  $\mu\text{m}$ , and supported by a cargo net structure at the top of a stainless steel vessel. This balloon system hangs in an 18 meter-diameter stainless steel spherical vessel. A buffer oil (BO) mixture of dodecane and isoparaffin fills the volume between the stainless steel vessel and the balloon in the buffer region. The density of the BO is kept at 0.04% lower than that of the LS, increasing its buoyancy, to reduce the weight-load on the balloon. The entire inner surface of the vessel, the inner detector (ID), is covered by an array of a total of 1879 photomultiplier tubes (PMTs). The fluor in the scintillator is excited by the energy loss of the

radiation generated from particle interactions, and emits light which is detected by the PMTs. A 3 millimeter thick acrylic barrier at 16.6 meter-diameter prevents radon emanating from PMT glasses from invading into the LS. This central detector stands in a cylindrical rock cavity. The volume between the sphere vessel and the cavity is filled with roughly 3200 cubic meters of pure water where 225 PMTs are placed to detect cosmic-ray muons by their Cerenkov light. This outer detector (OD) absorbs  $\gamma$ -rays and neutrons from surrounding rock (Suzuki et al. 2005). Figure 1-2 shows a conceptual drawing of the detector and labels the major components.

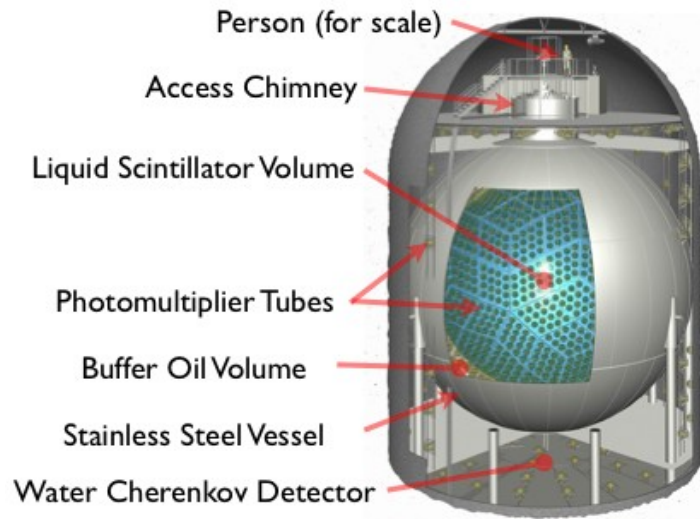


*Figure 1-2. Conceptual drawing of KamLAND.*

### 1.3 Purification System of the Detector

One kiloton of liquid scintillator is necessary in KamLAND because high statistics is essential to the observation of neutrinos. In addition, the sensitivity for the difference in the squared-mass of the neutrino mass states involved,  $\Delta m^2$ , strongly depends on the observed neutrinos. Therefore, better energy resolution as well as a low background environment is

essential for the experiment and to realize this, very low radioactive impurities for the low background experiment and high light yield for a good energy resolution (Tajima 2003). Lower background levels are required to detect solar neutrinos, so a new purification system was designed and tested.

Two methods were adopted for the new purification system: distillation for metallic or ionic chemicals, such as  $^{40}\text{K}$ , and purging for gaseous chemicals, such as  $^{85}\text{Kr}$ . The purification apparatus consisted of two storage tanks, three sets of distillation columns, and purge columns with an ultra-pure  $\text{N}_2$  generator. The three sets of distillation columns were for each of the three chemical components of the LS.

In May of 2007, the first purification campaign was started and ended in the beginning of August of 2007. The volumetric amount and flow rate of LS is shown in Figure 1-3 over the course of the purification campaign. LS was simultaneously withdrawn from the bottom plug of the balloon to be purified and then filled back into KamLAND from the top.

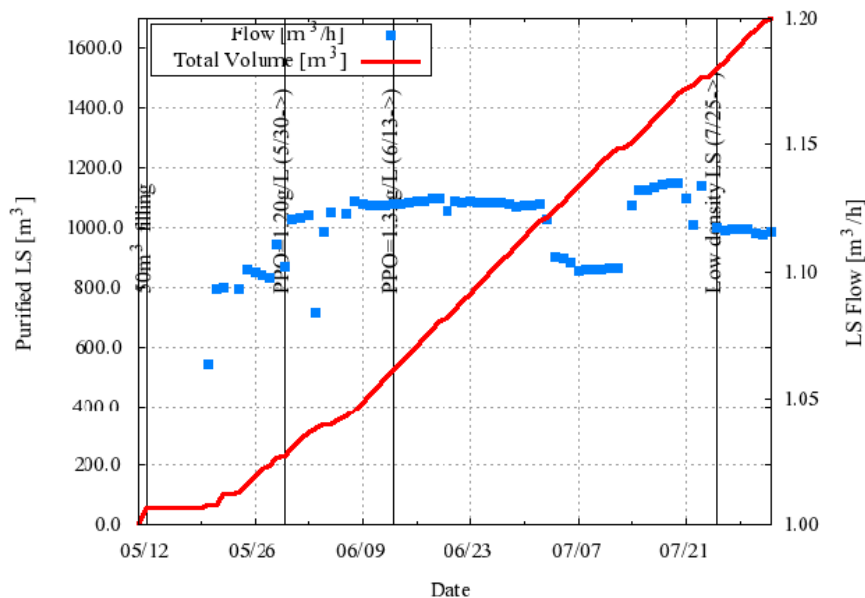


Figure 1-3. Purified LS volume and flow rate over 1st purification campaign.

During the purification, reduction factors of the radioactive concentrations were not as large as expected: one reason attributed was that the original unpurified scintillator and purified scintillator started mixing together. This was observed by tracing the movement of  $^{222}\text{Rn}$  daughters through  $^{214}\text{Bi}$ - $^{214}\text{Po}$  coincidence events. This process of tracking is explained in more detail in Appendix B. Another possibility was that the reduction factor itself in the purification apparatus appeared less than what was expected from small scale experiments (Kishimoto 2007). The concentrations of the radioactive impurities before and after the purification campaign are displayed in Table 1-1 as collected by the KamLAND Collaboration.

*Table 1-1. Background activities in KamLAND before and after purification.*

Isotope	Before [Bq/m <sup>3</sup> ]	After (Upper) [Bq/m <sup>3</sup> ]	After (Lower) [Bq/m <sup>3</sup> ]	Required [ $\frac{\text{After}}{\text{Before}}$ ]
$^{210}\text{Bi}$	$(4.2_{-0.6}^{+0.8}) \times 10^{-2}$	$(2 \pm 1) \times 10^{-4}$	$(1.0 \pm 0.1) \times 10^{-2}$	$10^{-6}$
$^{40}\text{K}$	$(4.4 \pm 0.4) \times 10^{-5}$	NA	$(1.3 \pm 0.1) \times 10^{-5}$	$10^{-6}$
$^{85}\text{Kr}$	$(5.1_{-0.4}^{+0.2}) \times 10^{-1}$	$(1.4_{-0.2}^{+0.1}) \times 10^{-2}$	$(1.85_{-0.02}^{+0.01}) \times 10^{-1}$	$10^{-5\sim 6}$
$^{222}\text{Rn}$	$2.8 \times 10^{-8}$	$1 \times 10^{-4}$	$1 \times 10^{-4}$	$< 10^{-3}$

To try to deal with the issue, the density and the temperature of the last 173 cubic meters of purified LS was changed:  $\Delta\rho = -0.03\%$  and  $\Delta T = +1.0\text{K}$ . These changes were made to provide a more distinct separation between the new and old LS with the density and temperature and resulted in the two layers: upper layer ( $z > 4\text{ m}$ ) and lower part ( $z > 2\text{ m}$ ) (Kishimoto 2007). This defined interface between the new and old LS can be seen in Figure 1-4, where the scale on the right has units of  $\text{mBq/m}^3$ . The dark blue area above the 3.5 meter border line has low energy

events occurring and indicates the newly purified LS. The desired purification is one where the interface between the old and new LS remains stratified (horizontal), so that no mixing occurs and only old LS is withdrawn from the detector.

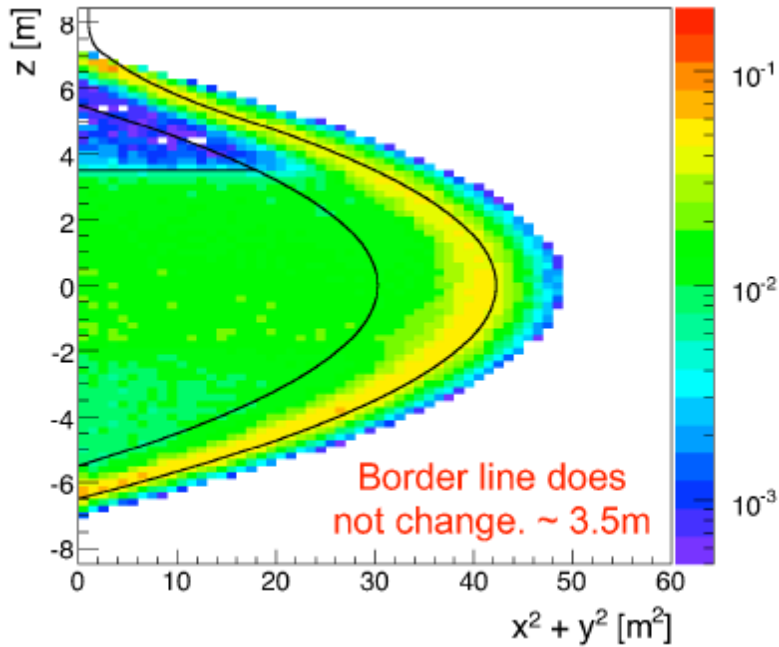


Figure 1-4. Distinct separation of old and new LS during first purification phase.

The reduction in the level of radioactive impurities during the first purification campaign was not sufficient to be able to observe the low energy  ${}^7\text{Be}$  solar neutrinos.

After the failure of the first purification campaign, steps were taken to upgrade some of the purification apparatus in preparation for the second purification campaign. It was hoped that with the upgraded control devices, more stringent temperature control and more careful adjustment of the liquid scintillator density would keep the new and old liquid scintillator boundary, minimizing mixing. In addition to the upgrades, purification parameters were

searched again to reduce the radioactive chemical much more effectively and use their values for the next purification campaign. It was also decided that for the second purification that the filling would occur from the bottom in the hopes of keep the interface stratified between the old and new LS. The second purification campaign occurred from June of 2008 to December of 2008, and again due to the presence of mixing, the desired reduced concentrations of the radioactive impurities were not met.

#### 1.4 Objective of Project

It is the aim of this project to develop a computational fluid dynamics (CFD) simulation of the detector using the commercial CFD software ANSYS® FLUENT to accurately simulate the mixing observed during this first purification process. From this CFD simulation, it is hoped that an efficient purification process can be developed to minimize the amount of mixing occurring, thus obtaining the desired reduction levels of the radioactive impurities.

#### 1.5 Scope of Project

The failures of the first two purification campaigns to meet their reductions in purities were results of the unexpected fluid flow and its effect on mixing the purified and unpurified scintillator. It appeared as if, due to the differences in density and temperature, natural convection was occurring that prevented the desired stratification during purification. Due to the expenses involved with operating the KamLAND project and the limited time frame of the project, multiple purification campaigns are not an option. CFD studies similar in nature (Jing, Xiao, & Zhou 2005) have been conducted concerning natural convection and stratification of fluid flows that would have otherwise been too costly or dangerous to perform.

Using a robust program like FLUENT, it should be possible to create a CFD simulation that can model transient flow, account for natural convection, and track the interface of the old

and new liquid scintillator over the period of the purification program. With the appropriate physical models and solution parameters chosen that can closely model the observed behavior of the first purification program; the simulation can then be used to run variations of the third purification program planned for July 2009 to obtain the most efficient process. The variations consist of changing the density and temperature of the purified LS, with the aim of obtaining a horizontally stratified, distinct interface inside the detector by minimizing natural convection. These variations can easily be incorporated into the CFD simulation.

## CHAPTER 2 CFD PHYSICAL MODELS

### 2.1 CFD Introduction

The Navier-Stokes equations form the basic mathematical model in fluid mechanics and describe a large variety of phenomena of fluid flow occurring in hydro- and aerodynamics, processing industry, biology, oceanography, meteorology, geophysics, and astrophysics. Computational Fluid Dynamics (CFD) concerns the digital/computational simulation of fluid flow by solving the Navier-Stokes equations numerically (Stein, de Borst, & Hughes 2004). The use of computational CFD programs by the engineering community has drastically increased over the past years. This rise in interest has resulted from improvements in the predictive capabilities of codes, reductions in costs of workstation technology, and inflation costs to perform experiments. For a large portion of the mechanical engineering community, the primary source of CFD capabilities is through the purchase of a commercial CFD code (Freitas 1993). Current CFD programs, such as the ANSYS<sup>®</sup> FLUENT software used in this research, can evaluate fluid flows involving complex geometries and a range of conditions, from subsonic to sonic flows as well as compressible or incompressible flows. It also has the ability to track multiple flows involving different phases, known as multiphase flow.

The use of CFD simulations has multiple advantages when dealing with experimental processes that can be performed virtually requiring less expenditure of resources, both in terms of capital and manpower, than would be needed to perform a physical experiment of the process. With a CFD simulation, it is readily available to modify the physical properties (density, viscosity, specific heats, etc.) of the materials, the boundary conditions and/or operating

conditions to achieve the desired results. It was not feasible to perform the physical process multiple times due to costs and time constraints involved with experiment.

In the CFD simulation of the KamLAND, heat and mass transfer will be modeled. The heat transfer will have components of conductive and convective heat transfer, as well as the effect of flow due to natural convection driven by the force of buoyancy which results from density differences in the fluid occurring due to temperature gradients. The CFD simulation will also use the VOF liquid-liquid model to track the volume fraction of and visualize the boundary interface of the old and new LS during the purification process.

Typical applications of the VOF model include the prediction of jet breakup, the motion of large bubbles in a liquid, the motion of liquid after a dam break, and the steady or transient tracking of any liquid-gas interface. In this case, the unpurified and purified LS will be treated as immiscible liquids to determine mixing. Few VOF studies were found that would be relevant to this project due to its unique conditions and geometry of concentric spheres.

## 2.2 Governing Equations

A physical understanding of the fundamental governing equations of fluid dynamics (the continuity, momentum, and energy equations) and of the terms associated with the equations is required to accurately set up the CFD simulation, even to properly interpret the results. The boundary conditions, and sometimes the initial conditions, dictate the particular solutions to be obtained from the governing equations (Anderson 1995).

With a working knowledge of the fundamental governing equations of fluid dynamics, CFD programs specializing in various flows, depending on the type of problem and method of solution, can be utilized. There are guides that help users to familiarize with CFD programs. Fluent User's Guide and FLUENT courses are very helpful to learn the elemental steps needed to

properly represent and post process a planned simulation. The next section contains the governing equations and assumptions made that are pertinent to the project.

### *2.2.1 Assumptions to Simplify the CFD Simulation*

When creating a CFD simulation, assumptions can be made to simplify the physical equations solved and reduce the amount of calculations to be computed. Because the geometry of the KamLAND project is mostly symmetric around a center axis of rotation, a 2D axisymmetric model can be used to represent the 3D model. This greatly reduces the size of the mesh used in the simulation. The inlet pipe used to transport the newly purified LS to the top of the chimney of the detector is located perpendicular to the center axis and would not be considered axisymmetric. To be able to model the problem as axisymmetric, the inlet pipe was removed from the geometry of the mesh and it was assumed that the purified LS uniformly flowed from the 2 meter-diameter section of the chimney, which is axisymmetric and was set as the inlet. Another assumption concerning the 2D axisymmetric model was that there would not be any circumferential (or swirl) flow occurring within the detector.

The Boussinesq approximation model, used in the solving of natural convection flows, was another assumption used in the governing equations to gain faster convergence of the solution. This model allows density to be treated as a constant instead of as a function of temperature in most of the equations. This assumption is valid for natural convection flows with small temperature differences in the domain of the flow.

### *2.2.2 The Mass Conservation and Momentum Equations*

For all flows, FLUENT (User Guide Sec. 9.2) solves conservation equations for mass and momentum. For flows involving heat transfer or compressibility, and additional equation for

energy conservation is solved. The equation for conservation of mass, or the continuity equation, for 2D axisymmetric geometries, can be written

$$\frac{\partial \rho}{\partial t} + \frac{\partial}{\partial x} (\rho v_x) + \frac{\partial}{\partial r} \rho v_r + \frac{\rho v_r}{r} = S_m \quad (1)$$

where  $S_m$  is the mass added to the continuous phase from the dispersed second phase, for this project equal to zero,  $\rho$  is the density,  $x$  is the axial coordinate,  $r$  is the radial coordinate,  $v_x$  is the dimensional axial velocity, and  $v_r$  is the dimensional radial velocity. The derivation of Equations 1-3 can be found in any undergraduate level of engineering fluid mechanics textbook. For 2D axisymmetric geometries, the axial, Equation 2, and the radial, Equation 3, momentum conservation equations are defined as

$$\begin{aligned} \frac{\partial}{\partial t} (\rho v_x) + \frac{1}{r} \frac{\partial}{\partial x} (r \rho v_x v_x) + \frac{1}{r} \frac{\partial}{\partial r} (r \rho v_r v_x) = & -\frac{\partial p}{\partial x} + \frac{1}{r} \frac{\partial}{\partial x} \left[ r \mu \left( 2 \frac{\partial v_x}{\partial x} - \frac{2}{3} (\nabla \cdot \vec{v}) \right) \right] \\ & + \frac{1}{r} \frac{\partial}{\partial r} \left[ r \mu \left( \frac{\partial v_x}{\partial r} + \frac{\partial v_r}{\partial x} \right) \right] + F_x \end{aligned} \quad (2)$$

and

$$\begin{aligned} \frac{\partial}{\partial t} (\rho v_r) + \frac{1}{r} \frac{\partial}{\partial x} (r \rho v_x v_r) + \frac{1}{r} \frac{\partial}{\partial r} (r \rho v_r v_r) = & -\frac{\partial p}{\partial r} + \frac{1}{r} \frac{\partial}{\partial x} \left[ r \mu \left( \frac{\partial v_r}{\partial x} + \frac{\partial v_x}{\partial r} \right) \right] + \\ & \frac{1}{r} \frac{\partial}{\partial r} \left[ r \mu \left( 2 \frac{\partial v_r}{\partial r} - \frac{2}{3} (\nabla \cdot \vec{v}) \right) \right] - 2 \mu \frac{v_r}{r^2} + \frac{2}{3} \frac{\mu}{r} (\nabla \cdot \vec{v}) + \rho \frac{v_z^2}{r} + F_r \end{aligned} \quad (3)$$

where

$$\nabla \cdot \vec{v} = \frac{\partial v_x}{\partial x} + \frac{\partial v_r}{\partial r} + \frac{v_r}{r} \quad (4)$$

$p$  is the static pressure,  $v_z$  is the swirl velocity, and  $F$  are any external body forces.

### 2.2.3 The Energy Equation and Heat Transfer Theory

The flow of thermal energy from matter occupying one region in space to matter occupying a different region of space is known as heat transfer. The physical models to be used in the project will be used to solve for conduction, convection, and the more complex heat transfer concerning buoyancy-driven flows, or natural convection. The heat transfer will be calculated in both solid and liquid regions. FLUENT (User Guide Sec. 13.2.1) solves the energy equation in the following form

$$\frac{\partial}{\partial t}(\rho E) + \nabla \cdot (\vec{v}(\rho E + \rho)) = \nabla \cdot \left( k_{eff} \nabla T - \sum_j h_j \vec{J}_j + (\bar{\tau}_{eff} \cdot \vec{v}) \right) + S_h \quad (5)$$

where  $k_{eff}$  is the effective conductivity ( $k + k_t$ , where  $k_t$  is the turbulent thermal conductivity, defined according to the turbulence model being used), and  $\vec{J}_j$  is the diffusion flux of species  $j$ .

The first three terms on the right-hand side of Equation 5 represent energy transfer due to conduction, species diffusion, and viscous dissipation, respectively.  $S_h$  includes the heat of chemical reaction, and any other volumetric heat that are defined in the CFD simulation.

In Equation 5,

$$E = h - \frac{p}{\rho} + \frac{v^2}{2} \quad (6)$$

where for physical models of the project for incompressible flows

$$h = \sum_j Y_j h_j + \frac{p}{\rho} \quad (7)$$

In solid regions, the energy transport equation has the following form

$$\frac{\partial}{\partial t}(\rho h) + \nabla \cdot (\vec{v} \rho h) = \nabla \cdot (k \nabla T) + S_h \quad (8)$$

where  $h$  is equal to sensible enthalpy,  $\int_{T_{ref}}^T c_p dT$ . The second term on the left-hand side represents convective energy transfer due to rotational or translational motion of the solids and will be neglected for this simulation.

#### *2.2.4 Natural Convection and the Boussinesq Model*

When heat is added to a fluid and the fluid density varies with temperature, a flow can be induced due to the force of gravity acting on the density variation. Such buoyancy-driven flows are termed natural convection flows and can be modeled by FLUENT (User Guide Sec. 13.2.5). The phenomenon of natural convection in an enclosure is as varied as the geometry and orientation of the enclosure (Bejan 2004). Buoyancy-induced flows are complex because of the essential coupling between the flow and transport equations. The first unified and comprehensive review of this subject was made by Ostrach (1964). Later summaries were presented by Ede (1967) and Gebhart (1979) and other reviews were compiled by Ostrach(1972), Catton (1978), Ostrach (1982), and Hoogendoorn (1986). Each of the last three emphasizes essentially different aspects of the subject of traditional natural convection problems in enclosures. There have been more recent studies using commercial CFD software, like FLUENT, that demonstrated natural convection in various real world problems (O'Malley 2003) and (Campbell 2002).

The ratio of the Grashof and Reynolds number in Equation 9 is a measure of the importance of buoyancy forces in a mixed convection flow and is defined as

$$\frac{Gr}{Re^2} = \frac{g\beta\Delta TL}{\nu^2} \quad (9)$$

where  $g$  is the gravitational constant,  $\nu$  is the kinematic viscosity, or  $\nu = \mu/\rho$ ,  $\Delta T$  is the difference in temperature,  $L$  is the length scale, and  $\beta$  is the thermal expansion coefficient

$$\beta = -\frac{1}{\rho} \left( \frac{\partial \rho}{\partial T} \right)_p \quad (10)$$

In pure natural convection, the strength of the buoyancy-induced flow is measured as by Rayleigh number

$$\text{Ra} = \frac{g\beta\Delta TL^3\rho}{\mu\alpha} \quad (11)$$

where  $\mu$  is the dynamic viscosity and  $\alpha$  is the thermal diffusivity

$$\alpha = \frac{k}{\rho c_p} \quad (12)$$

Rayleigh numbers less than  $10^8$  indicate a buoyancy-induced laminar flow, with transition to turbulence occurring over the range of  $10^8 < \text{Ra} < 10^{10}$ .

Natural convection flow is the result of varying fluids densities, usually as a function of temperature. To gain faster convergence of a solution in CFD, the Boussinesq approximation is used to treat the density term as a constant value in all solved governing equations, except for the buoyancy terms in the momentum equations defined in Equations 2 and Equation 3. The Boussinesq approximation  $\rho = \rho_0 (1 - \beta\Delta T)$  is used to eliminate  $\rho$  from the buoyancy term. This approximation is accurate as long as changes in actual density are small; specifically the Boussinesq approximation is valid when

$$\beta(T - T_0) \ll 1 \quad (13)$$

The physical properties of LS:  $\beta = 9.53 \times 10^{-4} \text{ 1/K}$  and  $T_0 = 15 \text{ }^\circ\text{C}$ . In the domain, the max temperature difference from the reference temperature is  $5 \text{ }^\circ\text{C}$ , so Equation 13 is satisfied:

$$9.53 \cdot 10^{-4} \frac{1}{\text{K}} \times (5 \text{ K}) = 4.77 \cdot 10^{-3} \ll 1$$

It is advised against using the Boussinesq model if there are large temperature gradients in the domain (FLUENT User Guide Sec. 13.2.5).

### 2.2.5 Volume of Fluid (VOF) Theory

There are a few multiphase models available for use in FLUENT. The aim of this project is to develop a multiphase flow regime consisting of a liquid-liquid stratified flow of two immiscible fluids separated by a clearly-defined interface. The Volume of Fluid (VOF) model theory is advised by FLUENT (User Guide Sec. 23.2.2) as a straightforward choice for stratified flows. In the VOF model, a single set of momentum equations is shared by the fluids, and the volume fraction of each of the fluids in each computational cell is tracked throughout the domain.

The tracking of the interface between the phases is accomplished by the solution of a continuity equation for the volume fraction of one or more of the phases. For the  $q^{\text{th}}$  phase, FLUENT (User Guide Sec. 23.3.2) defines this equation of tracking the interface in the following form

$$\frac{1}{\rho_q} \left[ \frac{\partial}{\partial t} (\alpha_q \rho_q) + \nabla \cdot (\alpha_q \rho_q \vec{v}_q) \right] = S_{\alpha_q} + \sum_{p=1}^n (\dot{m}_{pq} - \dot{m}_{qp}) \quad (14)$$

where  $\dot{m}_{qp}$  is the mass transfer from phase  $q$  to phase  $p$  and  $\dot{m}_{pq}$  is the mass transfer from phase  $p$  to phase  $q$ .  $S_{\alpha_q}$  is the mass source term, but default by zero. When the VOF model is turned on in FLUENT, a primary-phase is selected. The volume fraction equation will not be solved for the primary phase; the primary phase volume fraction will be computed based on the following constraint

$$\sum_{q=1}^n \alpha_q = 1 \quad (15)$$

The single momentum equation solved throughout the domain and the resulting velocity field is shared among the phases. The momentum equation shown below in Equation 16 is dependent on the volume fractions of all phase through the properties  $\rho$  and  $\mu$ .

$$\frac{\partial}{\partial t}(\rho \vec{v}) + \nabla \cdot (\rho \vec{v} \vec{v}) = -\nabla p + \nabla \cdot [\mu(\nabla \vec{v} + \nabla \vec{v}^T)] + \rho \vec{g} + \vec{F} \quad (16)$$

One limitation of the shared-fields approximation is that in cases where large velocity differences exist between the phases, the accuracy of the velocities computed near the interface can be adversely affected (FLUENT User Guide Sec. 23.3.4).

The energy equation, also shared among the phases, is shown below.

$$\frac{\partial}{\partial t}(\rho E) + \nabla \cdot (\vec{v}(\rho E + p)) = \nabla \cdot (k \nabla T) + S_h \quad (17)$$

The VOF model treats energy, E, and temperature, T, as mass-averaged variables

$$E = \frac{\sum_{q=1}^n \alpha_q \rho_q E_q}{\sum_{q=1}^n \alpha_q \rho_q} \quad (18)$$

where  $E_q$  for each phase is based on the specific heat of that phase and the shared temperature.

The properties  $\rho$  and  $k_{eff}$  (effective thermal conductivity) are shared by the phases. Because the energy equation also utilizes the shared-fields approximation, if large temperature differences between the phases, the accuracy of the temperature near the interface is limited.

## CHAPTER 3 CFD KAMLAND MODEL

### 3.1 Steps in Solving CFD Problem

Once the scope and details of a CFD project have been identified, there are a series of steps FLUENT outlines that need to be completed to obtain in order to run a successful CFD model. The steps are shown below.

1. Define the modeling goals.
2. Create the model geometry and grid.
3. Set up the solver and the physical models
4. Compute and monitor the solution.
5. Examine and save the results.
6. Consider revisions to the numerical or physical model parameters, if necessary.

### 3.2 The Modeling Goals

The purpose of this project is to obtain a CFD simulation of the KamLAND detector that can first verify the validity of its results by producing realistic physical models of what is known about the detector when it is not undergoing purification and what was observed during the past purification programs. Second, the model needs to be robust in order to compute the month and a half (or longer) purification process within a short time frame, preferably a week to coincide with the rebooting of the servers that house the CFD software. Third, the model needs to be able to be modified to try various methods of constraining the mixing that is observed: changing rates of flow, varying the density to alter buoyancy forces, changing values of temperature of the purified LS, etc.

### 3.3 Creating the Model Geometry

To create an accurate model of the KamLAND detector, the engineering drawings used in the design and construction of KamLAND were provided and used as a basis for all dimensions created. The schematic in Figure 3-1 displays all of the major parts of the detector: the liquid scintillator (LS), the buffer oil (BO), the inner detector (ID), and the outer detector (OD) or antiwater.

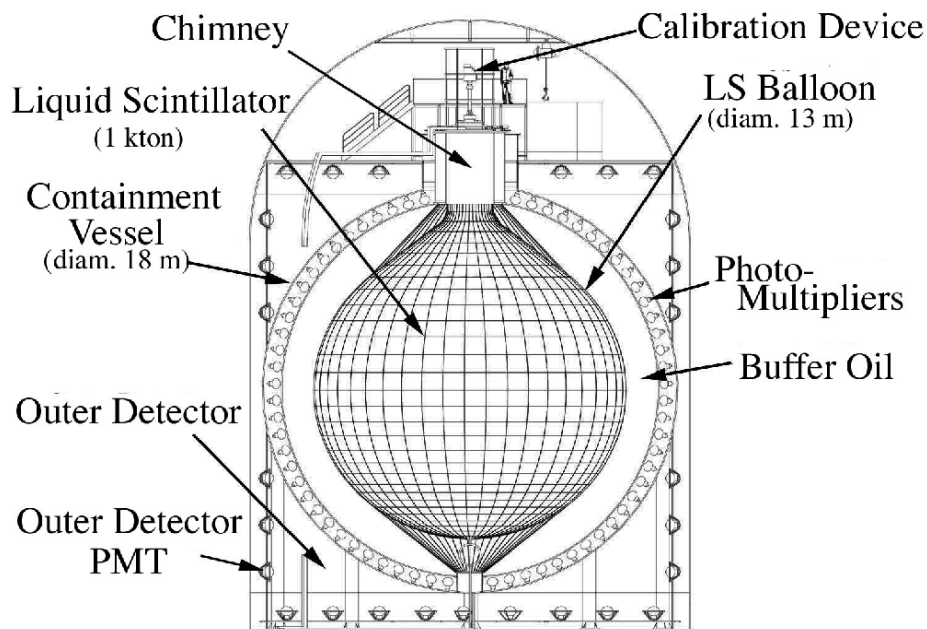


*Figure 3-1. KamLAND detailed schematic.*

Because of familiarity and ease of use, the commercial computer aided drawing (CAD) software Pro/Engineer WildFire 4.0 (Pro/E) was used to create the complex solid geometry of the concentric spheres curves, detector chimney, and the cylindrical outer detector. The solid model created by Pro/E is shown in Figure 3-2.

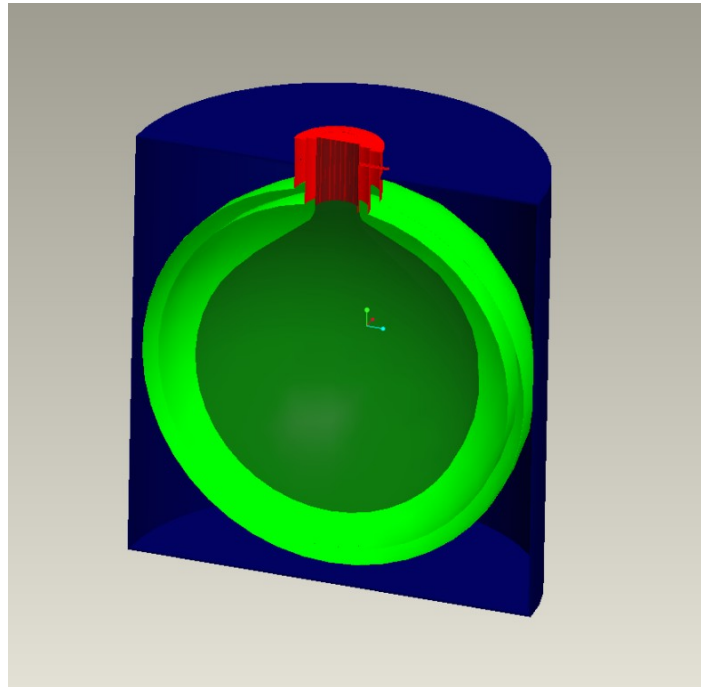


*Figure 3-2.* KamLAND geometry created using Pro/E.

The next step is to use the Pro/E model and export the geometry, using the neutral data format IGES that allows the digital exchange of data among CAD programs, to a grid generator. The IGES file of was read into the grid generator program GAMBIT (Geometry and Mesh Building Intelligent Toolkit). GAMBIT is a single, integrated preprocessor for CFD analysis (and can also be used to create geometry, but is not as versatile as Pro/E). Due to inconsistencies between the tolerances of the two CAD programs, the detector geometry had to be “healed” to get rid of any hanging nodes or disconnected faces by using the Boolean operations of the program. The “healed” geometry created by GAMBIT is shown in Figure 3-3. GAMBIT is then used to simplify the geometry, mesh this simplified geometry, and assign boundary conditions.

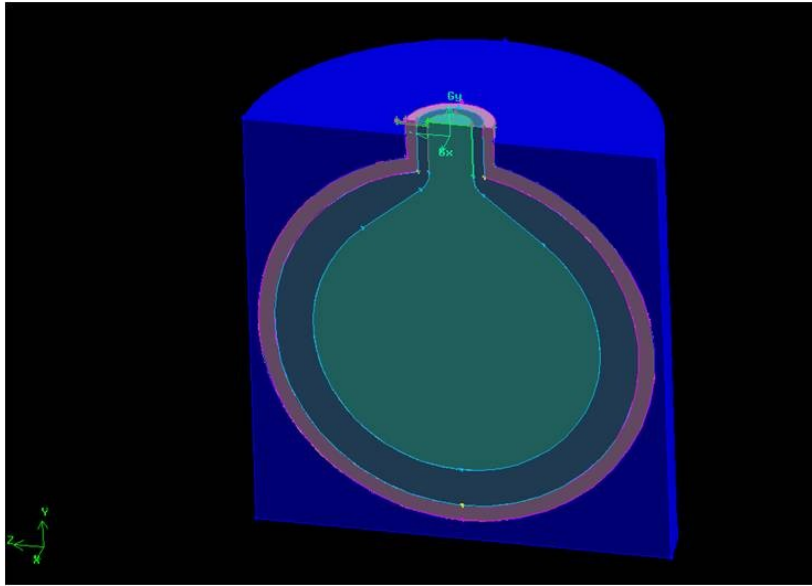


Figure 3-3. GAMBIT geometry created from IGES file.

### 3.3.1 Simplifying the KamLAND Geometry

The major parts of the KamLAND experiment are separated by walls whose thicknesses are small with respect to the overall geometry. Meshing these walls with solid cells would lead to high-aspect-ratio meshes and a significant increase in the total number of cells. Instead, these solid walls are represented in GAMBIT by an edge that is assigned a “wall” boundary condition used by FLUENT. FLUENT will solve a 1D conduction equation to compute the thermal resistance offered by the wall, using the thickness and the thermal conductivity of the material assigned to the wall.

Another simplification of the geometry shown in Figure 3-3 is to convert the 3D geometry into a 2D face for use in an axisymmetric, 2D model. This assumption was previously described in Section 2.2.1 and greatly reduces the number of cells required for the CFD simulation. The simplified geometry obtained is displayed in Figure 3-4. The geometry in Figure 3-4 was also

rotated so that the axis that the geometry will be revolved around lies along the x-axis. This is a condition required by FLUENT when using the 2D axisymmetric model. The centers of the spheres correspond to the origin of the system, with the positive z-axis pointing upward toward the dome.

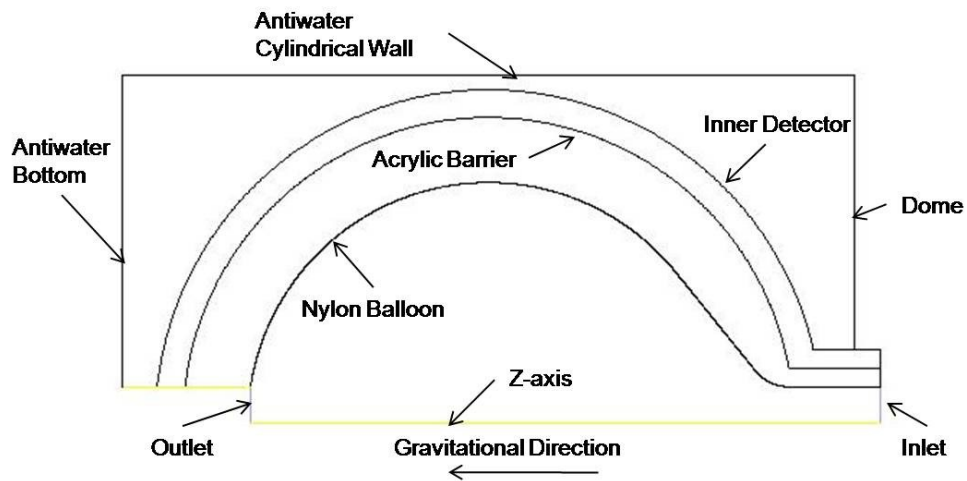


Figure 3-4. GAMBIT simplified geometry.

### 3.3.2 Meshing the KamLAND Geometry

The effect of resolution, smoothness, and cell shape of the mesh on the accuracy and stability of the solution process is dependent on the flow field being simulated. The resolution of the mesh describes the density of the nodes. A high resolution, or dense, mesh is required in the domain where the fluid flow is a result of natural convection to resolve any large gradients present. In regions of large gradients, it is important that the grid be fine enough to minimize the change in flow variables from cell to cell. The smoothness of the mesh describes the changes in cell volume between adjacent cells. Rapid changes results in large truncation errors, the

difference between the partial derivatives in the governing equations and their discrete approximations. The cell shape (the skewness and aspect ratio) also has a significant impact on the accuracy of the numerical solution. These three characteristics help quantify the quality of the mesh and result in a warning if certain criteria are not met. Another important consideration when meshing the geometry was the attachment of boundary layers along the edges in the domains where flow occurs. Boundary layers provide high resolution by defining the spacing of mesh node rows in regions immediately adjacent to edges and resolve the steep velocity gradients near the wall due to no-slip wall conditions (the velocity is assumed to be zero at the wall). For this project, since there were not any previous similar CFD simulation studies, there was no way to estimate what resolution of the mesh was required.

In order to obtain this required resolution, mesh independence is required. This means that increases in the resolution of the mesh, or increasing the density of the mesh, will not have any effect on the calculated flow field solution, but will only increase the computational expense. From earlier meshes created, there appeared to be a correlation between the size of the grid and the mass continuity residuals. In one case with low mesh resolution, large mass continuity residuals of  $10^{+6}$  were observed and would not reduce below  $10^{+3}$ . The convergence criterion for the mass continuity residual is  $10^{-3}$ . To better understand this correlation, a very simple geometry was created to determine the resolution required. This geometry consisted of a sphere and cylinder of the same dimensions as the KamLAND detector and modeled as 2D axisymmetric. This simplified geometry is displayed in Figure 3-5. From the use of this geometry in CFD simulations, with conditions comparable to that of the KamLAND experiment, the mesh of the more complicated detector was developed. Trial and error resulted in the final

mesh used in the CFD simulation shown in Figure 3-6 (note that areas appear solid due to the highly dense mesh).

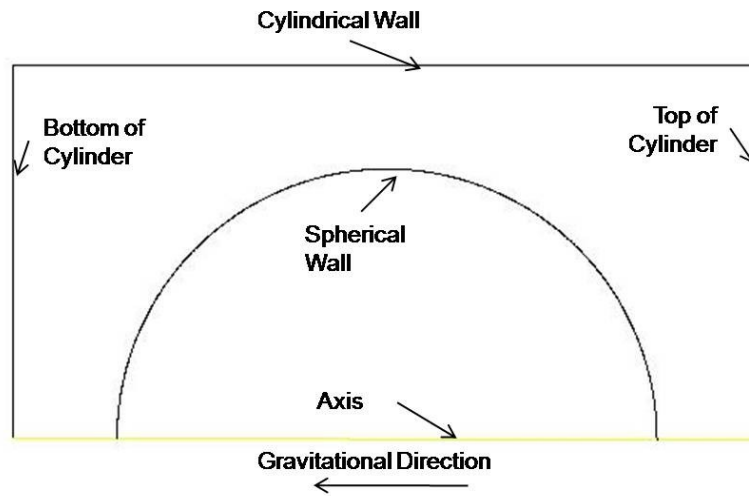


Figure 3-5. Simple geometry of model used to test the grid resolution required.

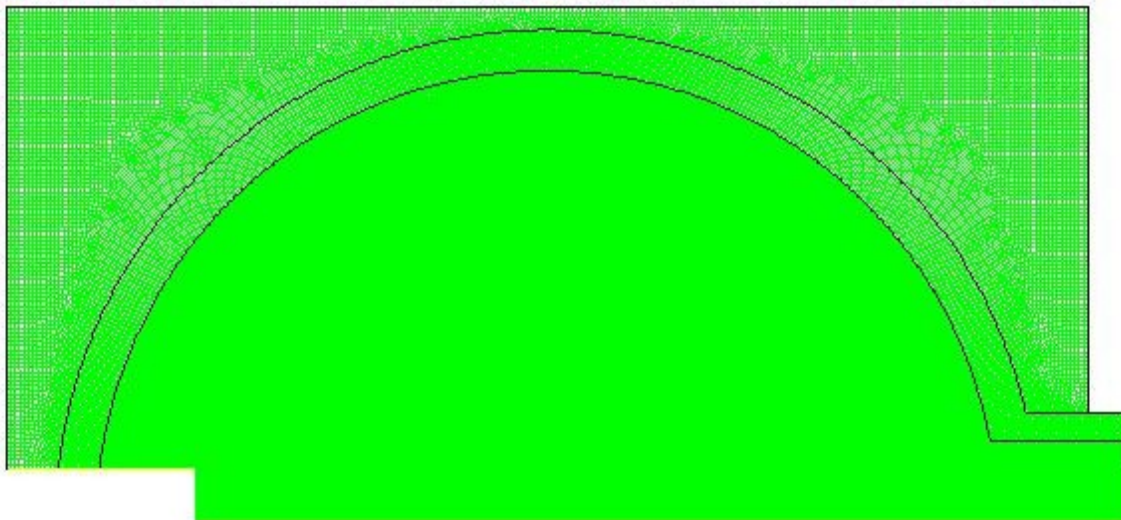
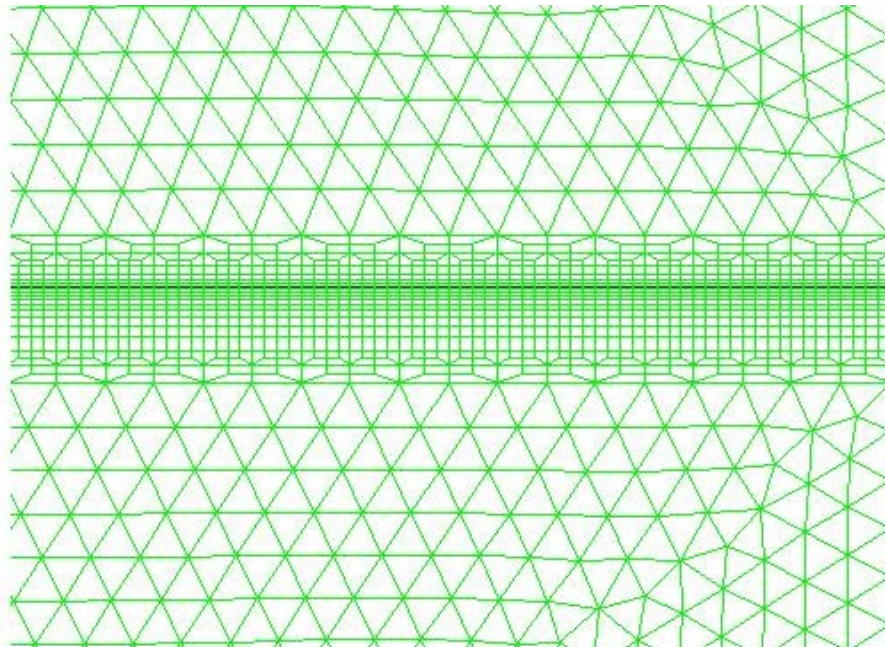


Figure 3-6. Mesh used in KamLAND CFD simulation.

A close up of the boundary layers that were attached to the walls next to fluid flow, in the domains of the LS, can be seen in Figure 3-7. The boundary layer captures the details of the boundary flow at the wall. In the figure of the boundary layer, there are two transition rows from the assignment of a transition patten of 4:2, where 4 is the mesh intervals in a given row and 2 is the number of mesh intervals in the immediately preceding full row. This helps the smoothness and skewness of the grid by controlling the transition of the quadrilateral cells of the boundary layer to the triangular cells of the domain mesh.



*Figure 3-7.* Enlarged view of the boundary layer used on the walls of the LS domain.

In Figure 3-6, the bottom of the balloon was simplified into a horizontal edge equal in dimension to the edge of the inlet located at the top detector. In earlier grids generated, the outlet was treated as a small-diameter pipe, but this presented troubles in controlling the velocity scale and produced highly skewed cells. The velocity scale of the inlet and outlet is determined by the

mass flow rate. The mass flow rate entering the detector is the same as the mass flow rate leaving the detector, with mass flow rate defined as

$$\dot{m} = \rho \cdot v \cdot Area \quad (19)$$

Because the mass flow rates are the same, a large decrease in the area of the outlet, compared to the area of the inlet, would result in a large increase of the velocity. With the outlet set to the same area as the inlet, the velocity at the top of the detector inlet is of the same magnitude as the velocity of the detector outlet at the bottom. To prevent the skewed cells produced, circled in Figure 3-8, the outlet edge was moved to the bottom of the detector.

With these skewed cells removed and the velocity scale controlled, the time required for the computation of each time step was greatly increased and the convergence of the solution was faster as well.

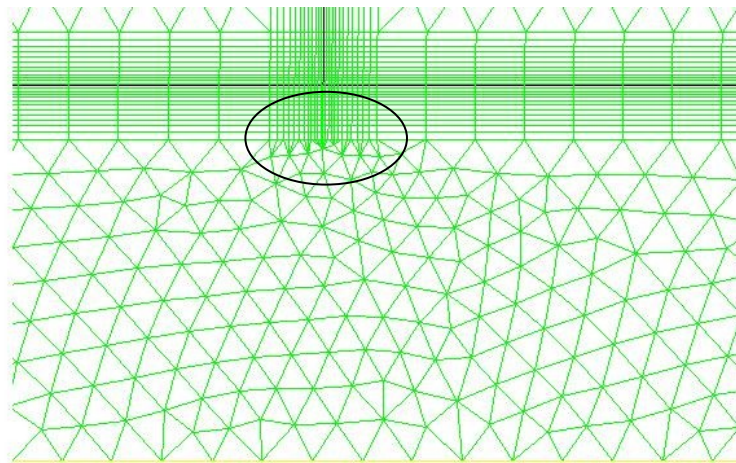


*Figure 3-8.* Enlarged view of skewed cells in outlet pipe.

### 3.3.3 Description of the Grid

The grid consists of four major parts of the detector: the LS, BO, ID, and OD. Because the direction of the flow field is not known and predicted to circulate inside of the domains, triangular meshing was used in the fluid domains of the LS, BO, and ID. Quadrilateral meshing was used in the OD, which is treated as a solid. Each domain was meshed using the Pave option, which creates an unstructured grid of mesh elements and was found not to create any errors when meshing the difficult curved geometry. The number of nodes and the number of elements of the four major parts of the detector that make up the faces are listed in Table 3-1.

Before exporting the 2D mesh to FLUENT, it is easier to go ahead and set the boundary conditions in GAMBIT and define the continuums. While exporting, GAMBIT will warn if there are any highly skewed cells, as they can greatly affect the convergence of the solution or the computational expense of the simulation.

*Table 3-1.* Details of the CFD mesh created in GAMBIT.

Face name	Number of nodes	Number of elements	Boundary layer
Liquid scintillator	262 235	463 896	Yes
Buffer oil	221 645	316 278	Yes
Inner Detector	69 928	111 656	No
Outer Detector	15 178	1 468	No
Total	568 986	893 298	N/A

### 3.4 Pre-Processing of FLUENT

#### *3.4.1 Reading in the Grid*

It is during the pre-processing phase of the CFD that the physical models and solvers are selected and supplied the necessary information. The first part of the pre-processing is reading in the mesh to be used for the simulation. Because the model is axisymmetric, no nodes can lie below the x-axis in FLUENT; as this would create a negative volume when FLUENT revolves the model around the axis. Performing grid check will display if there are any nodes that violate this. Again, because of the difference in the tolerances between GAMBIT and FLUENT, even though no nodes lie below the grid in GAMBIT, during the export a few nodes will be listed as below the axis. To easily correct this, translate the entire grid a small distance in the y-axis direction, and then translate the grid that same distance in the reverse direction, and the tolerances should be taken care of (note that this will not work if the double precision solver is selected).

#### *3.4.2 Defining the Material Properties and Boundary Conditions*

For the KamLAND project, the physical properties for all the major materials within the detector are needed to perform an accurate simulation and are provided in Appendix C. It is important to note that, to be able to model natural convection in the flow, the density for liquids used in the simulation must be set to either Boussinesq or be a function of temperature. The physical parameters of every boundary condition, assigned in GAMBIT and provided in Appendix D, also need to be supplied. The center of the balloon was set to an “axis” boundary condition as required for an axisymmetric case. The LS inlet of the detector, located at the top of the chimney, was set to “mass-flow inlet” with a mass flow rate of  $1.1 \text{ m}^3 / \text{hour}$ , recorded over the course of the first campaign as displayed in Figure 3-9. It should be noted that for 2D

axisymmetric problems, the mass flow rate assigned to the boundary condition is the flow rate through the entire ( $2\pi$ -radian) domain, not through a 1-radian slice.

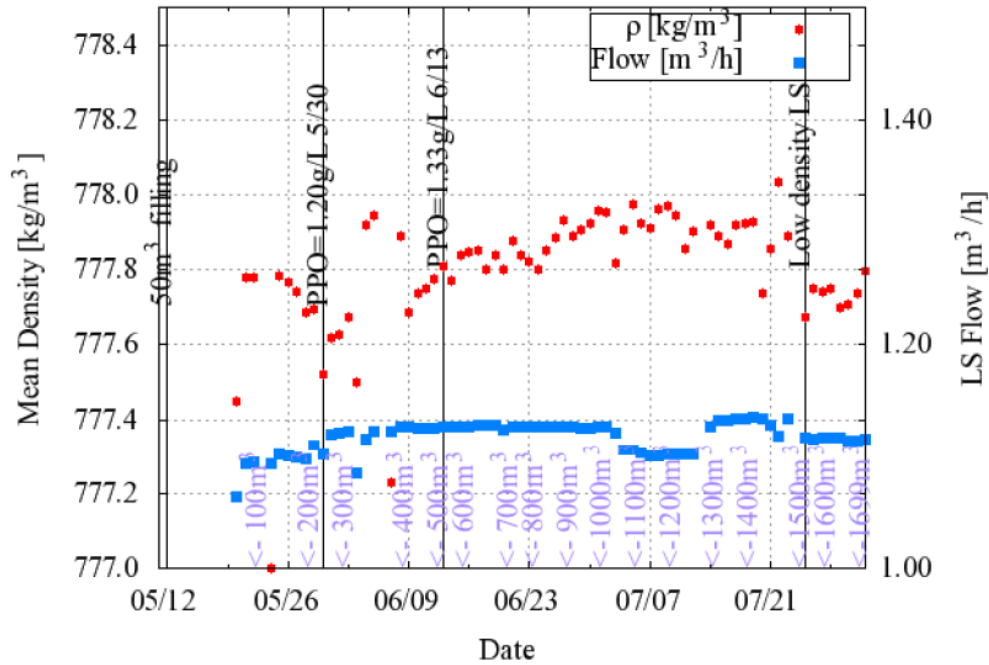


Figure 3-9. Density and mass flow rate of LS over the course of the first purification process.

To help the simulation along computationally by avoiding reverse flow on the edge where the LS is withdrawn, this outlet located at the bottom of the balloon was also set to a boundary condition of “mass-flow inlet,” with the same mass flow rate as the inlet. The major difference between the two: the axial component of the outlet was set to -1 to induce outflow. There were other boundary conditions that could be set for the inlet and outlet for the simulation. For the LS inlet, a “velocity inlet” could also have been specified. For the LS outlet, the edge could have been set as an “outflow” boundary condition, but this resulted in reverse flow on the edge and is also not recommended for use with multiphase models. The majority of the

remaining edges were set to “wall” boundary conditions, with thickness and material assigned. Details of the boundary conditions are listed in Appendix D.

The outer detector, or antiwater, posed a unique problem to the simulation. Outside of the cylindrical wall of the OD, the solid rock of the mine acts as a heat sink. There were not any measured temperature values of the OD’s walls to assign to the boundary condition. But, there were temperature measurements made of the water contained in the OD at various elevation levels, displayed in Figure 3-10. It can be observed that the bottom of the OD was consistently at 10° C, so this constant temperature was set as the boundary condition for the bottom edge of the OD.

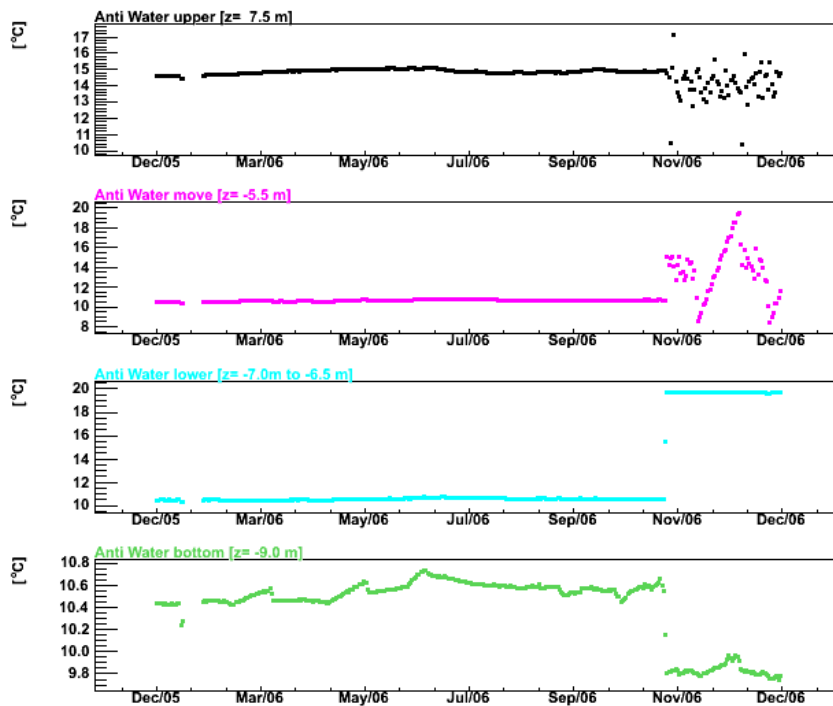


Figure 3-10. Plots of temperature versus time of four elevation levels within the OD.

But the cylindrical wall of the OD was not a constant temperature as the elevation increased. Since it was observed that the temperatures stayed fairly constant over time, each elevation was assigned a constant temperature measurement. A polynomial function was then fitted to the values for the elevations and their respective temperatures as displayed in Figure 3-11.

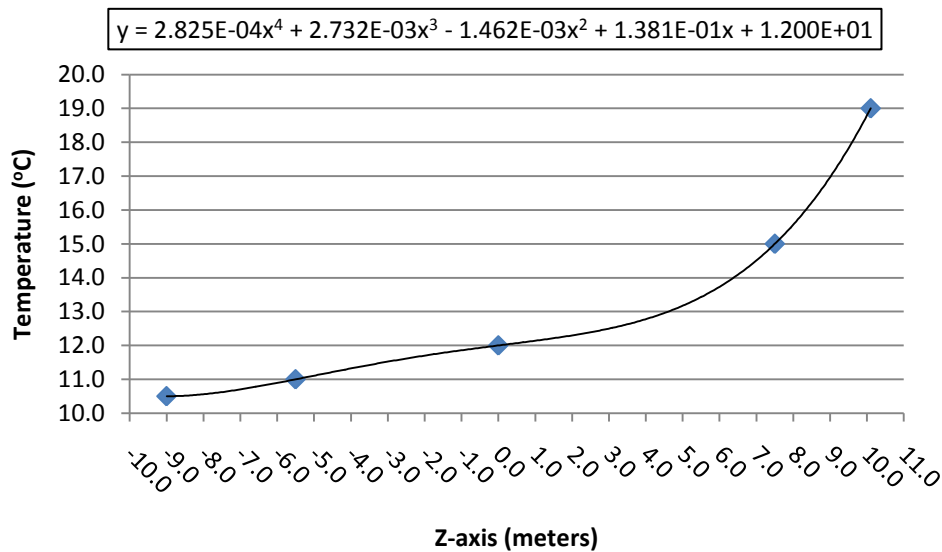


Figure 3-11. Polynomial trendline of OD temperature versus distance along z-axis.

This polynomial function was compiled into a user defined function (UDF), see Appendix E, to specify this temperature profile along the cylindrical wall of the OD. The temperature in the dome above detector was measured to be an average of 19 °C, so this was set as the constant temperature for the edge representing the wall between the OD and dome.

Another unique problem was the presence of the 1,911 photomultiplier tubes (PMTs) located on the stainless steel wall of the inner detector, behind the acrylic glass that separates the

buffer oil from the inner detector. The detected power of output of each PMT was estimated to be 0.4 Watts / PMT. Using the following formula

$$\dot{q} = \frac{N_{PMTs} \times P_{PMTs}}{V_{ODsphere}} = \frac{11911 \text{ PMTs} \times 0.4 \text{ W/PMTs}}{\frac{4}{3}\pi \times ((9m)^3 - (9-0.016m)^3)} = 47.0 \text{ W/m}^3 \quad (19)$$

a volumetric heat generation rate for the “wall” boundary condition representing the steel sphere of the ID was calculated to apply these heat sources to the model.

The continuum in each of the domains was assigned the appropriate material. In the OD, water was set as the material. The ID and BO domains contain a non-scintillating, ultra clear mineral oil and the domain of the LS detector contains the liquid scintillator. These material properties were created in the FLUEN materials database and are listed in Appendix C. To further simplify the program and from calculation run errors, it was decided to set the OD, ID, and BO domains as solids with the same thermal conductivity as their liquid counterparts. This assumption was made due to the stable temperature profile that had been measured over the course of the KamLAND project in each of these regions. This greatly helped computational time, as only the flow field for the LS needed to be calculated.

### 3.4.3 Enabling the Desired Physical Models

With all of the boundary conditions set, the next part of the pre-processing of CFD simulation is to set the physical models that will be calculated. In the operating conditions, the value for gravity is entered in the desired direction and a reference temperature is set for the Boussinesq parameter. The VOF simulation is the best choice for stratified and liquid-liquid flows, so the necessary parameters are selected or entered, such as the selection of the primary-phase (for this simulation, the unpurified LS is the best choice) and selection of the VOF implicit scheme due to the presence of gravity. When large body forces (e.g., gravity) exist in multiphase

flow, the body force and pressure gradient in the momentum equation are almost in equilibrium, with the contributions of convective and viscous terms small in comparison. Segregated algorithms converge poorly unless partial equilibrium of pressure gradient and body forces is taken into account (FLUENT User Guide 23.9.4).

### *3.4.5 Initializing the Solution*

With the VOF and natural convection physical models enabled, nothing was changed in the solver except to make sure the 2d axisymmetric was enabled. The next step was to initialize the solution, or set values to the grid that served as a starting point for the calculations. The temperature at the center of the detector is roughly 12.5 °C, so this was chosen as a good estimate for the temperature initialization value. For the KamLAND project, measurements have confirmed that during non-purification campaigns there was almost no flow, with velocity magnitudes around  $10^{-8}$  m/s, so values of zero are set for the radial and axial velocities' initialization values.

Because there was almost no flow present before the first purification process, the energy and flow equations could be decoupled; the energy equation was only solved to obtain a distributed temperature profile to act as an initial temperature profile for the transient calculations involving multiphase flow. This essentially turned the model into a heat transfer problem with conduction only. This method was found to obtained a temperature profile along the z-axis and inside of the detector that was very close to measurements taken along the z-axis and in the detector. A comparison of the temperature distribution measured in the KamLAND experiment before the purification process and the initial temperature distribution calculated before transient flow is displayed in Figure 3-12 and Figure 3-13, respectively.

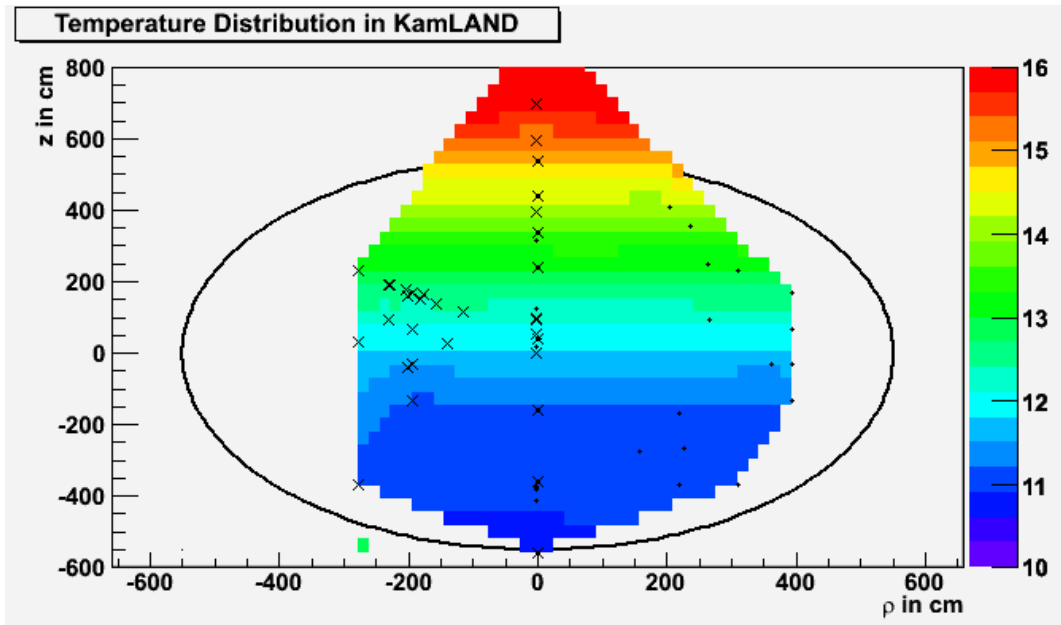


Figure 3-12. Measured temperature ( $^{\circ}\text{C}$ ) distribution in KamLAND.

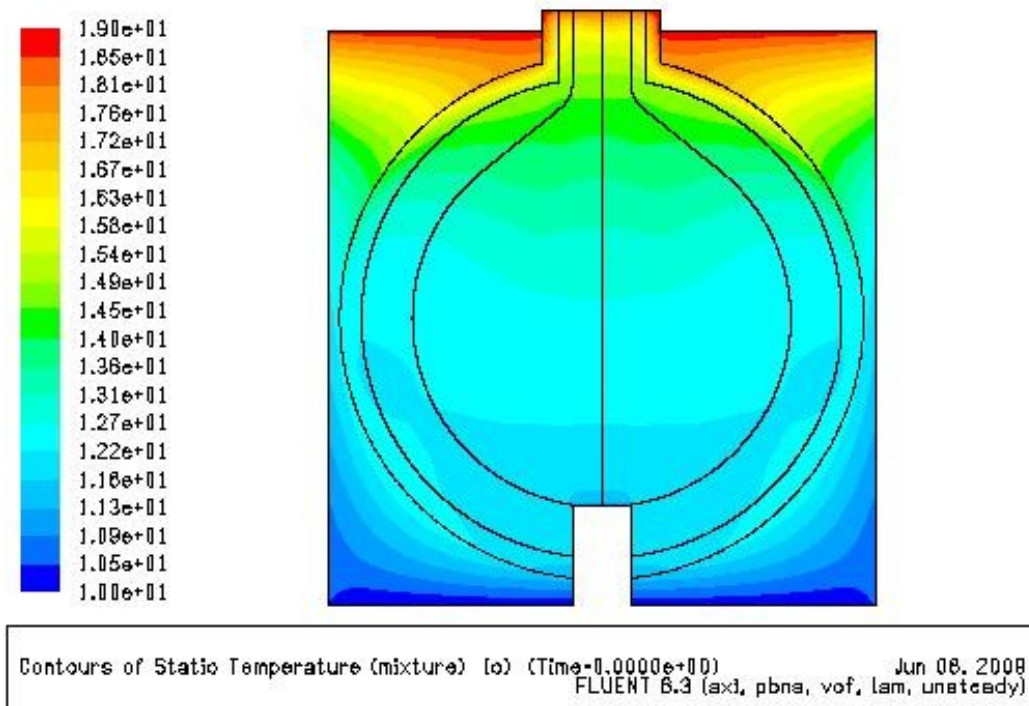


Figure 3-13. Initial temperature distribution calculated by FLUENT.

### 3.4.6 Selecting the Solution Controls

With the distributed temperature flow field solved, the next step was to couple the energy and flow equations and solve the simulation as a steady state problem. But with the more complex problem of flow and energy solved for, the multiple parameters in the solution controls needed to be assessed to obtain the right selection of the pressure-velocity coupling scheme, the appropriate discretization scheme, and the values for the under-relaxation factors of the variables solved: pressure, density, body forces, momentum, and energy. Because of the nonlinearity of the equation set being solved by FLUENT, it is necessary to control the change of  $\phi$ , or the variable being solved for. This is typically achieved by under-relaxation of variables (also referred to as explicit relaxation), which reduces the change of  $\phi$  produced during the iteration. In a simple form, the new value of the variable  $\phi$  within a cell depends upon the old value,  $\phi_{old}$ , the computed change in  $\phi$ ,  $\Delta \phi$ , and the under relaxation factor,  $\alpha$ , displayed below in

$$\phi = \phi_{old} + \alpha \Delta \phi \quad (20)$$

The FLUENT User's Guide provided some guidance on these choices, but most CFD problems are unique and there is no definite right answer about what choice is the best without selecting it and running the simulation. This was where closely monitoring the residuals (continuity, x and y-velocities, and energy) of the simulation during the iterations became important to observe the progress of the solution. Residuals (FLUENT User Guide 25.18) are a way to monitor the convergence of the solution; the solution is considered converged when these residuals have decreased to their defined criteria, usually dropping several orders of magnitude.

With the default solution controls selected, the steady state simulations with flow and energy coupled was slow to converge and produced unrealistic results. This can be seen in initial

temperature distribution seen in Figure 3-14, obtained as described in section 3.4.5, and a converged steady state solution with flow and energy coupled displayed in Figure 3-15.

Instead of a stratified thermal distribution that had been observed, the domains containing flow experienced thermal mixing that resulted in a mostly homogenous temperature profile throughout.

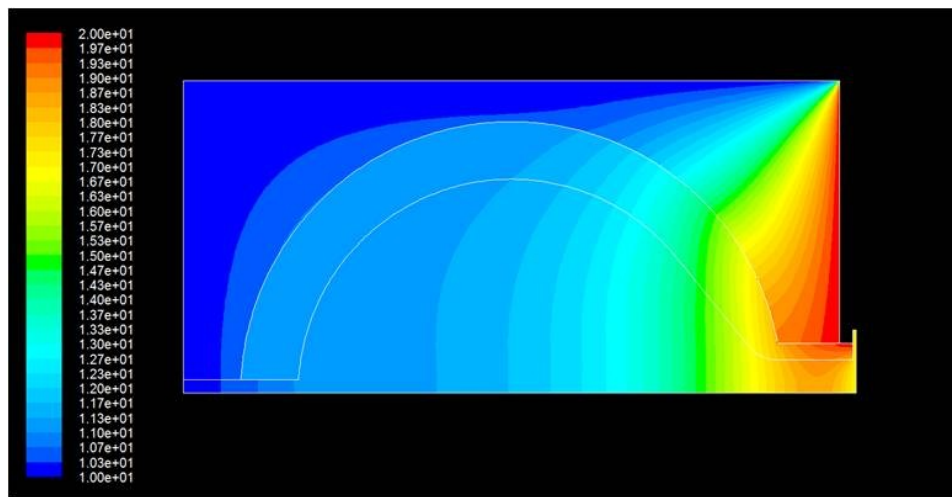


Figure 3-14. Temperature distribution of solution with only the energy equation solved.

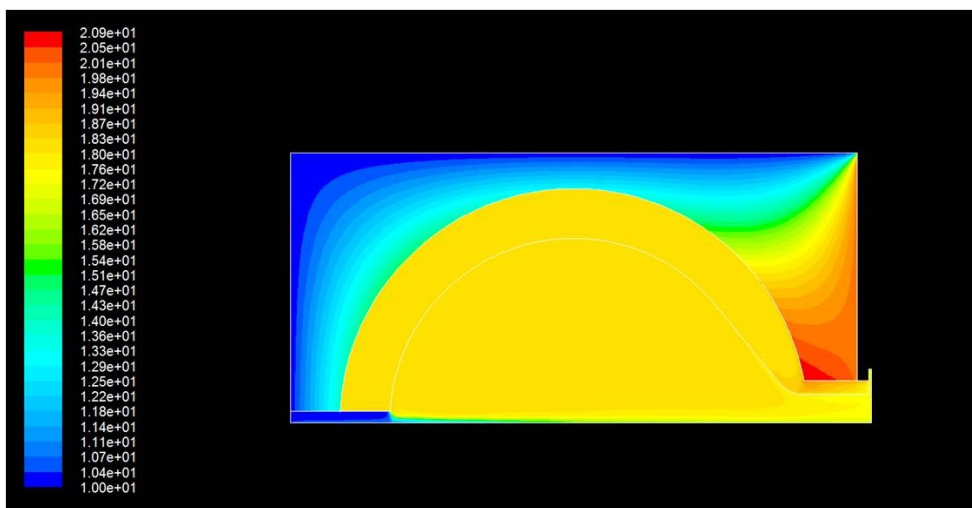


Figure 3-15. Temperature distribution with energy and flow equations coupled.

It was not understood what was creating the thermal mixing effect that should not have been present. As was the case for developing the necessary resolution for the grid, the simplified geometry in Figure 3-5 was used to model a simpler CFD simulation of natural convection, with a similar temperature profile and fluid conditions as that of the physical KamLAND experiment. It was also during this simpler simulation that the UDF temperature profile was implemented to more accurately reflect the measured temperature values of the OD. In the simplified simulation, the domain of the cylinder was treated as a solid with the thermal properties of water and the domain of the sphere was set as a liquid containing the LS. With only energy solved for, a distributed temperature profile was obtained and is displayed in Figure 3-16. With the default controls and flow and energy coupled, again, the converged steady state solution experienced homogenous thermal mixing but with the impossible event of viscous heating in the sphere that resulted in a temperature greater than the maximum temperature present. This is shown in Figure 3-17.

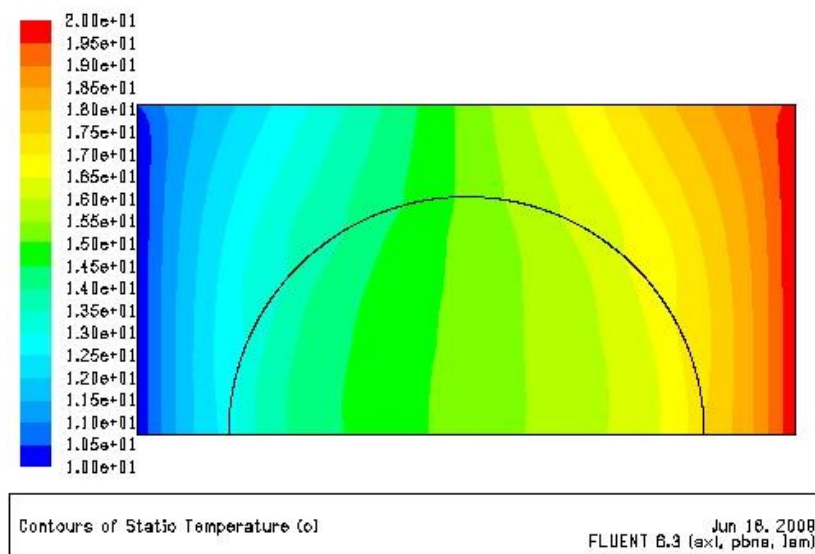


Figure 3-16. Temperature distribution in simple CFD model with only energy solved.

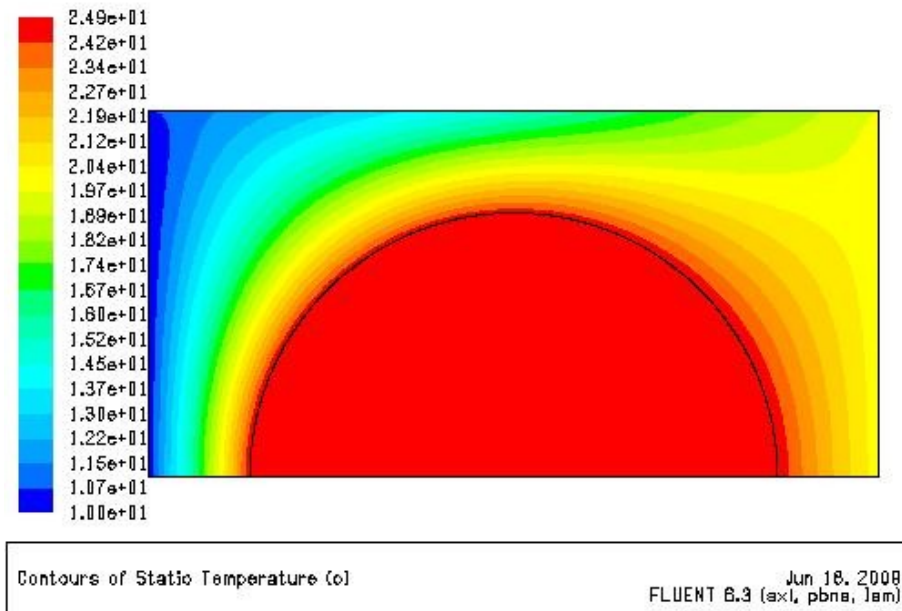


Figure 3-17. Temperature distribution in simple CFD model with energy and flow solved.

Upon further research and investigation, it was found that the reduction in the under-relaxation factor for the momentum variable is necessary to prevent unrealistic results and divergence. Because the velocity magnitudes are low, on the order of  $10^{-3}$  to  $10^{-5}$ , the under-relaxation factors help impede the amount of change in the momentum equations during iterations, helping convergence. For a natural convection problem, where the energy field impacts the fluid flow (via temperature dependent properties or buoyancy), a lower value for the under-relaxation factor, typically in the range of 0.8 to 1.0, was also found to be helpful. The use of the simple CFD model of natural convection helped to understand how the under-relaxation factors contributed a major role in obtaining a stable converged solution.

With the knowledge obtained concerning the discretization schemes and the under-relaxation factors, the next step was to solve a transient, multiphase solution of the purification process using the KamLAND geometry. FLUENT provides some guidance on solving a

multiphase system that is encountering some stability or convergence problems. If a time-dependent problem is being solved, and patched fields are used for the initial conditions, it is recommended to perform a few iterations with a small time step, at least an order of magnitude smaller than the characteristic time of the flow. And then increase the size of the time step after performing a few time steps.

### 3.5 Computing the Solution of FLUENT

The purification program at KamLAND lasted approximately a month and a half. While computing and monitoring the solution, this was kept in mind in order to make sure the time steps were large enough to account for the large amount of time that needed to be computed while keeping the solution stable. To help facilitate the processing of this large amount of time to be simulated, FLUENT's parallel solver was utilized with a 6-node cluster. The KamLAND grid was partitioned into 5 sections using the principal strip method, with the aim of an equal distribution of the LS flow domain in each partition, as displayed in Figure 3-18.

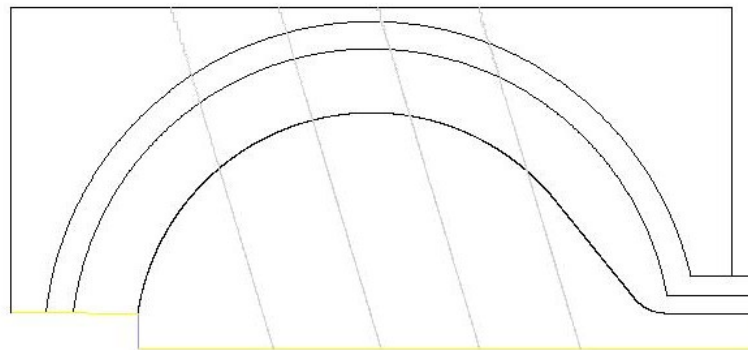


*Figure 3-18.* KamLAND geometry partitioned for parallel computing.

The time steps were steadily increased (from 0.1 seconds to 120 seconds) until an optimal time step was observed. Larger time steps would sometimes require longer computational effort and more time steps than that of a smaller time step calculated for the same span of time. Each time step should take approximately 5-15 iterations to converge for an efficient transient solution. The optimal time step of 120 seconds for the simulation resulted in twelve simulated days for a day of computation, making it possible to simulate approximately two months in a week of computation. For a stable, transient CFD simulation's residuals should appear to a saw-tooth pattern. This is seen the KamLAND CFD simulation's scaled residuals plot in Figure 3-19. See Appendix F for a work sheet maintained while the simulation was running.

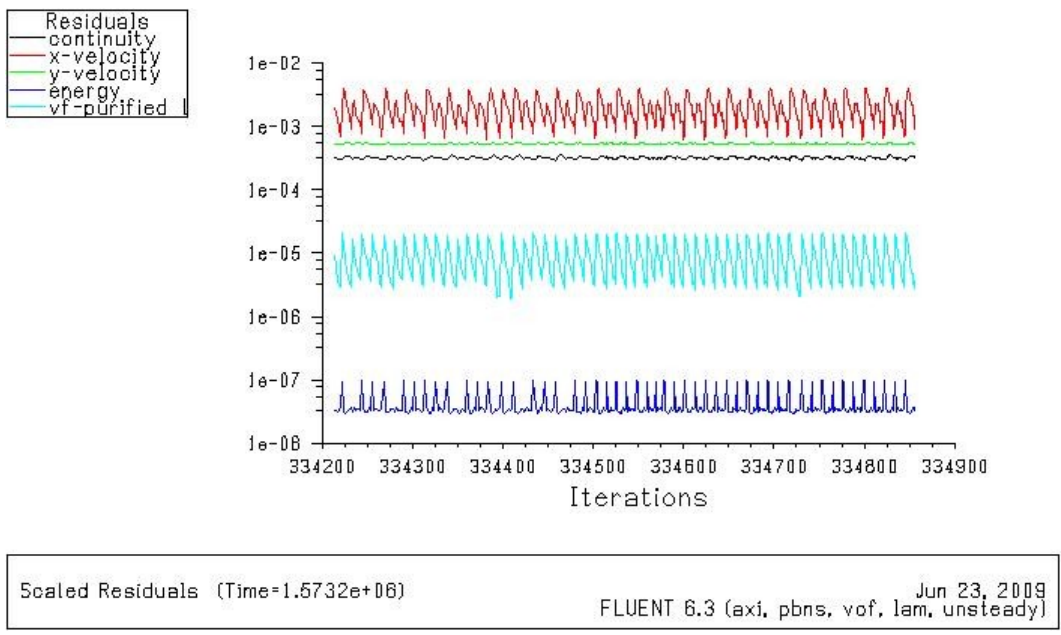


Figure 3-19. Scaled residuals plot of the KamLAND CFD simulation.

### 3.6 Post-Processing the Results of FLUENT

To be able to review data obtained in an experiment is very important to see if the goals of the experiment have been met. When a case file (or .cas file) of a simulation is written, it contains the mesh, material properties, boundary conditions, and the settings for the solver. This makes it easy to track changes made. To record the variables solved for at each node, a data (or .dat) file is created. Because much of this CFD simulation involved continuous, unmonitored computing time, FLUENT was set to automatically create a .dat file at specified time step intervals that amounted to four hours of flow time calculation. From this data file any of the contours can be readily accessible as well as any fluxes that may have been computed.

## CHAPTER 4 RESULTS AND DISCUSSION

The following figures from Figure 4-1 to Figure 4-10 are the results from the KamLAND CFD simulation that was ran as KamLAND\_2Dv10vof.cas and the details of this simulation is given in Appendix E. Figure 4-1 through Figure 4-9 display eight weeks of which purification of the LS was occurring. Figure 4-10 displays a week after purification was stopped and now flow entered or left the LS detector. The montage figures below each contain four figures: KamLAND  $^{222}\text{Rn}$  tracking, see Appendix B (top left), CFD contours of volume fraction [unpurified] (top right), CFD contours of velocity magnitude [m/s] (bottom left), and CFD contours of stream function [kg/s] (bottom right).

The top two figures in the montage cannot be compared directly, but the figure on the left serves as a reference. This is due to the fiducial volumes cuts used to normalize the  $^{222}\text{Rn}$  plot, as this is seen in the units of the horizontal axis of the plot. The three horizontal lines that appear in the FLUENT images of Figure 4-1 to Figure 4-10 serve as referential marking. The middle line lies at the center of the detector on the z-axis, and the lines above and below are each spaced 3.5 meters from this center. The montage in Figure 4-11 displays the temperature contours in chronological order, from left to right, top to bottom.

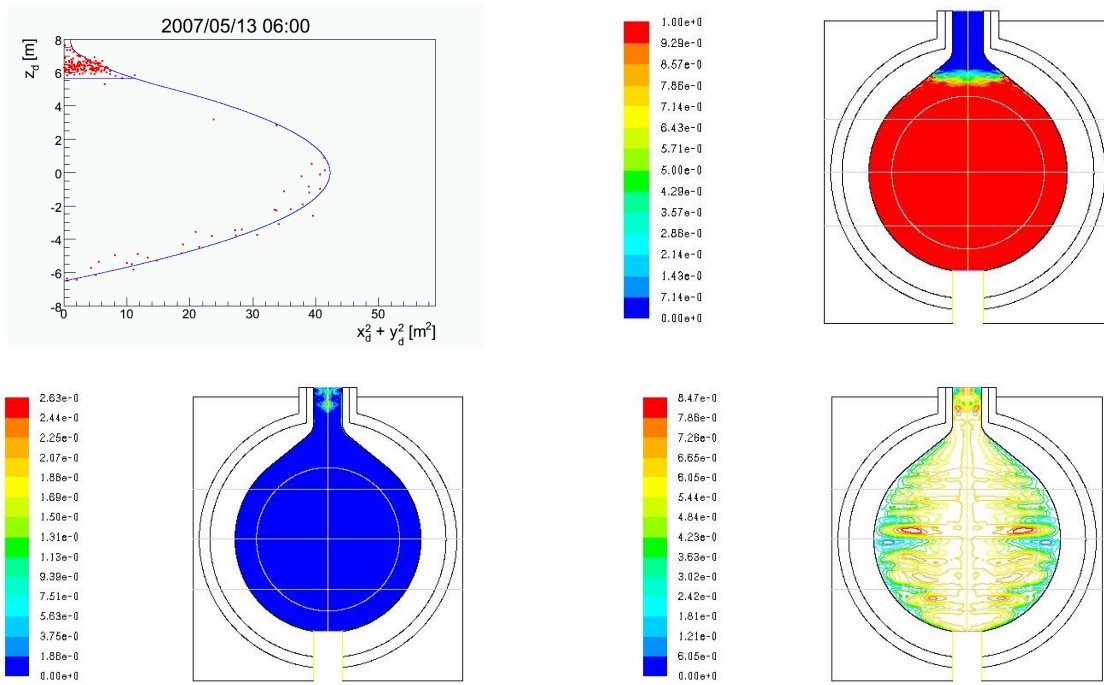


Figure 4-1. Montage of KamLAND after one day of purification.

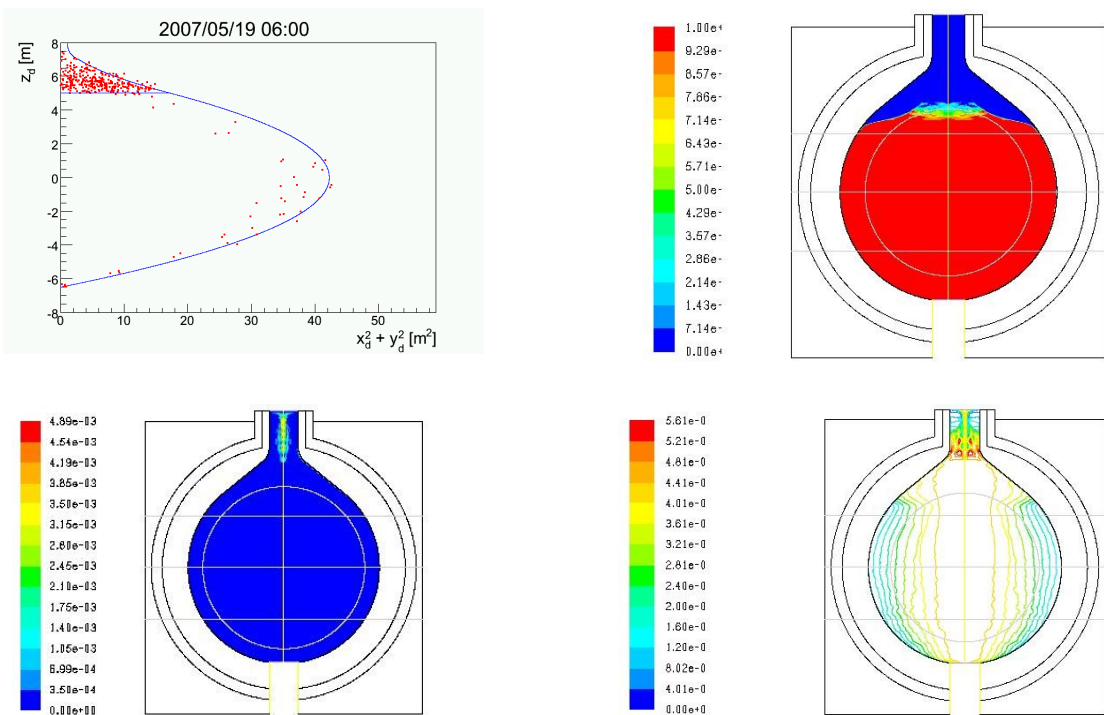


Figure 4-2. Montage of KamLAND after one week of purification.

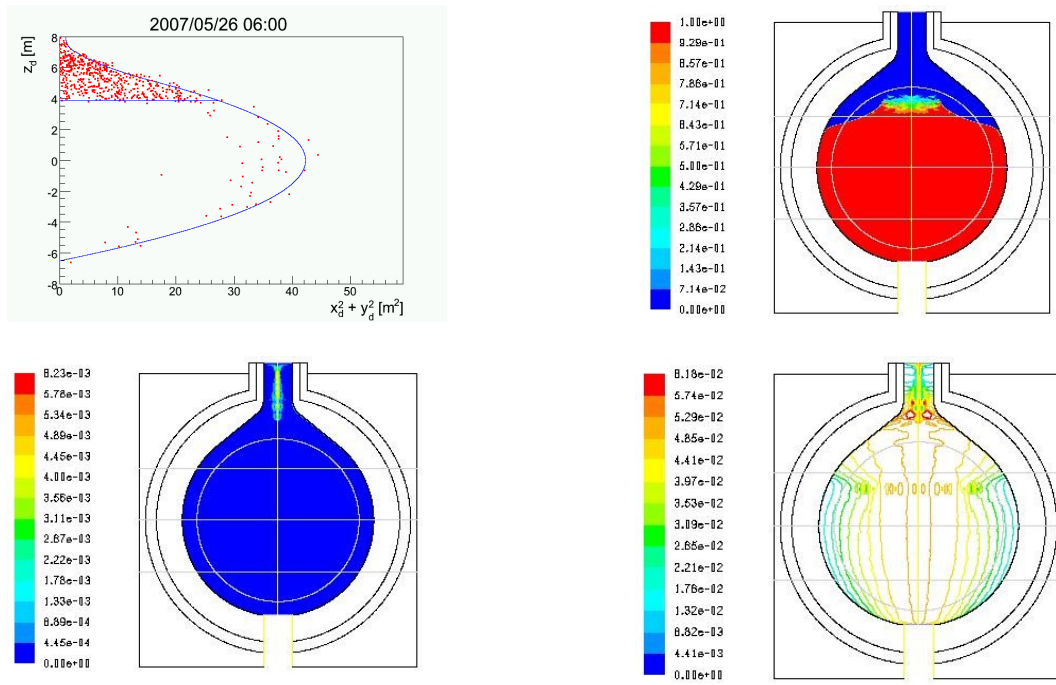


Figure 4-3. Montage of KamLAND after two weeks of purification.

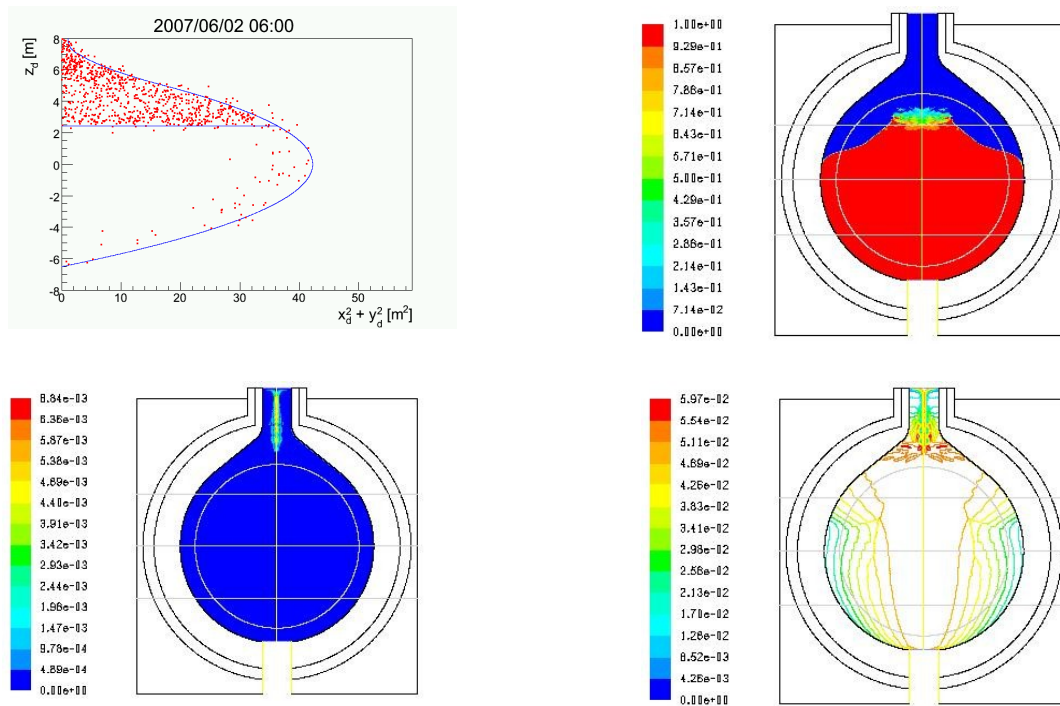


Figure 4-4. Montage of KamLAND after three weeks of purification.

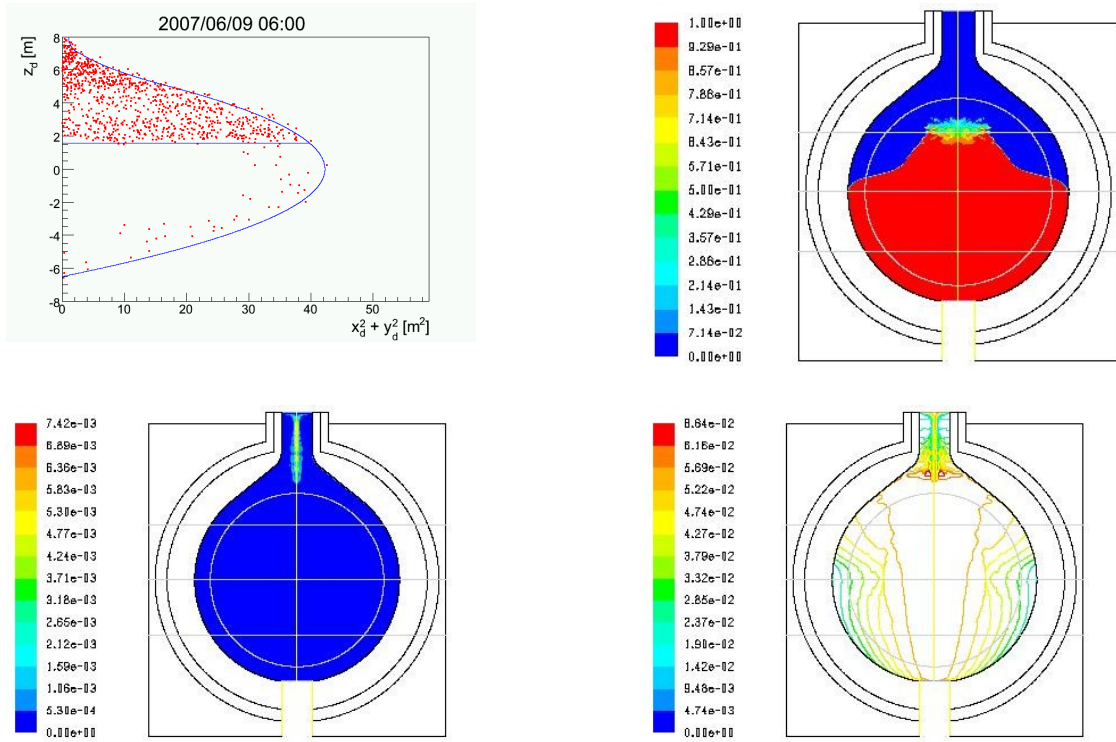


Figure 4-5. Montage of KamLAND after four weeks of purification.

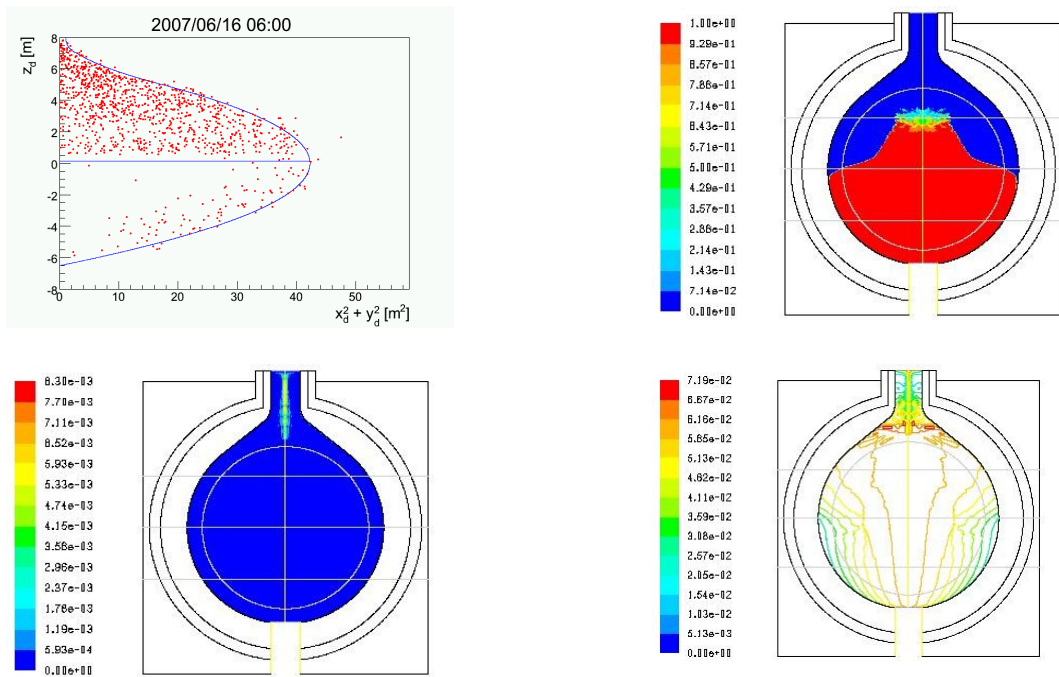


Figure 4-6. Montage of KamLAND after five weeks of purification.

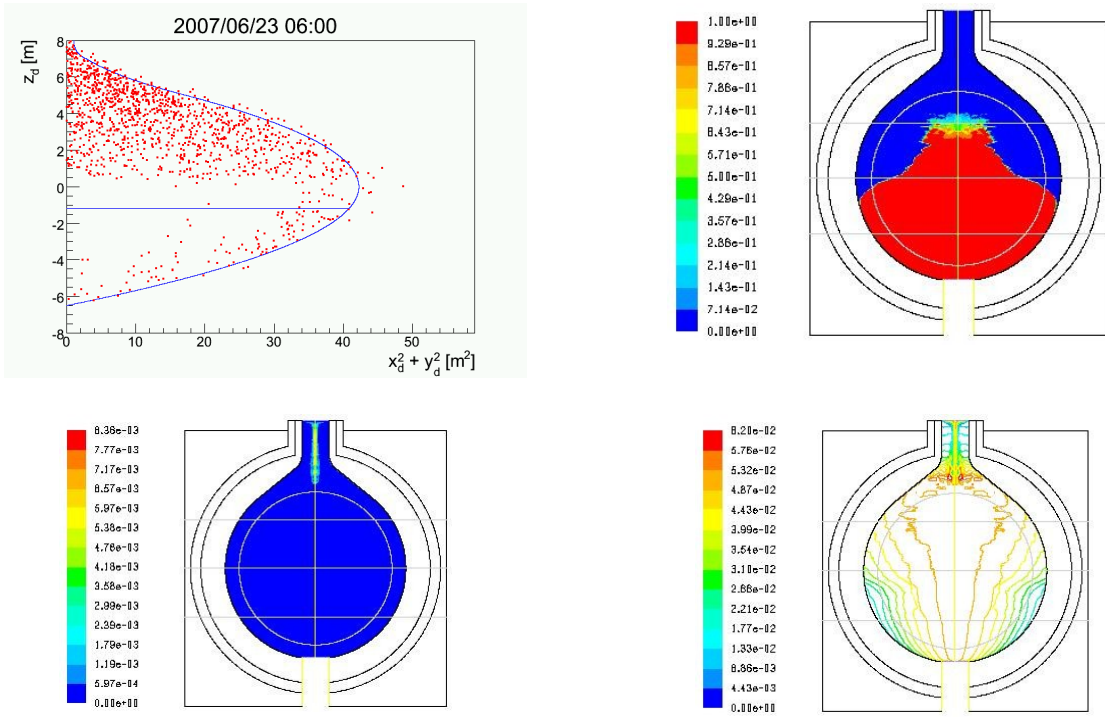


Figure 4-7. Montage of KamLAND after six weeks of purification.

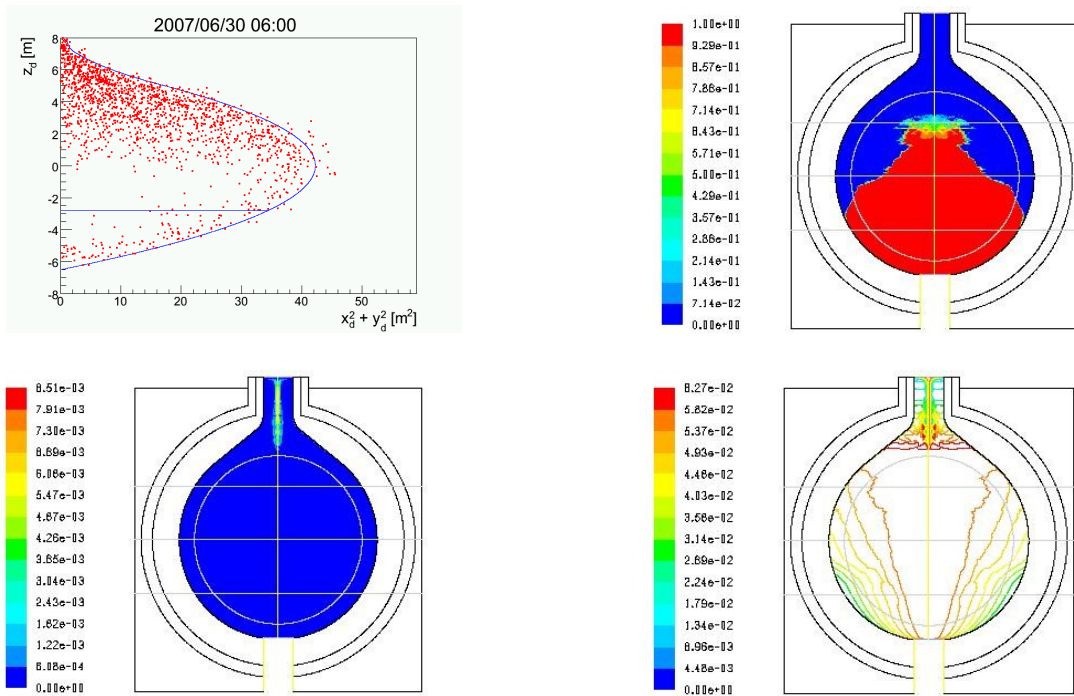


Figure 4-8. Montage of KamLAND after seven weeks of purification.

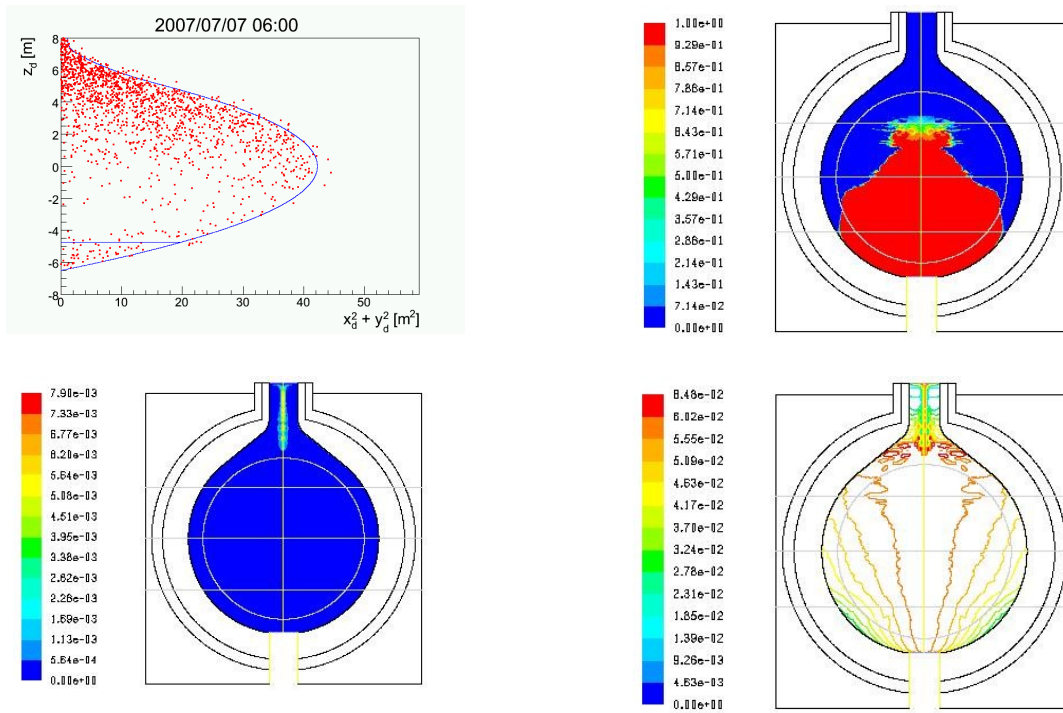


Figure 4-9. Montage of KamLAND after eight weeks of purification.

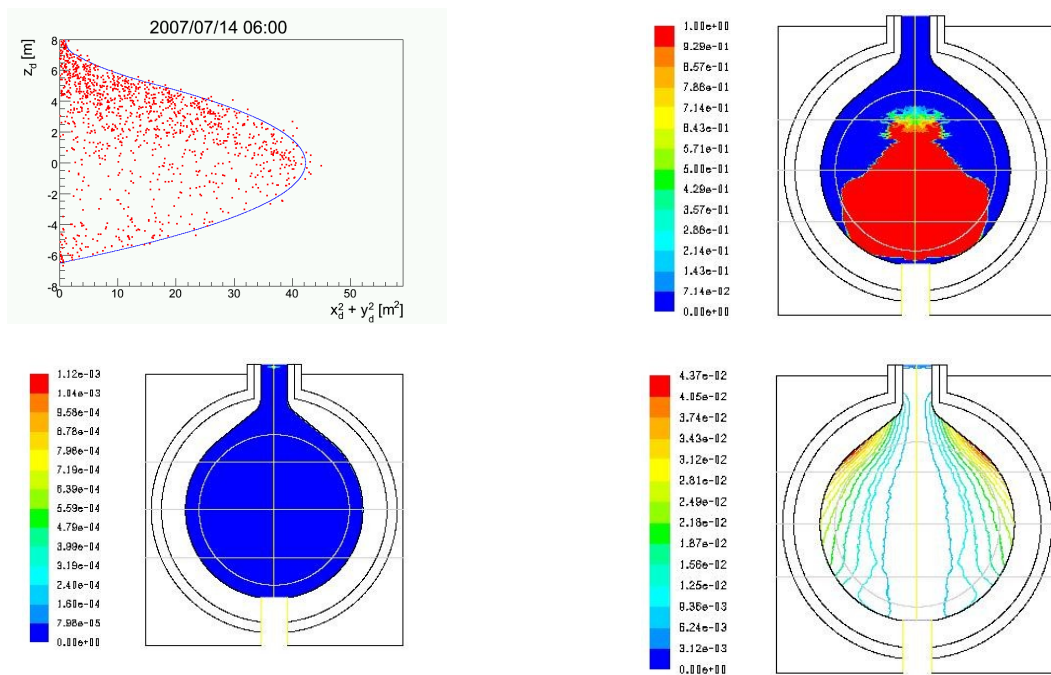


Figure 4-10. Montage of KamLAND after nine weeks of purification.

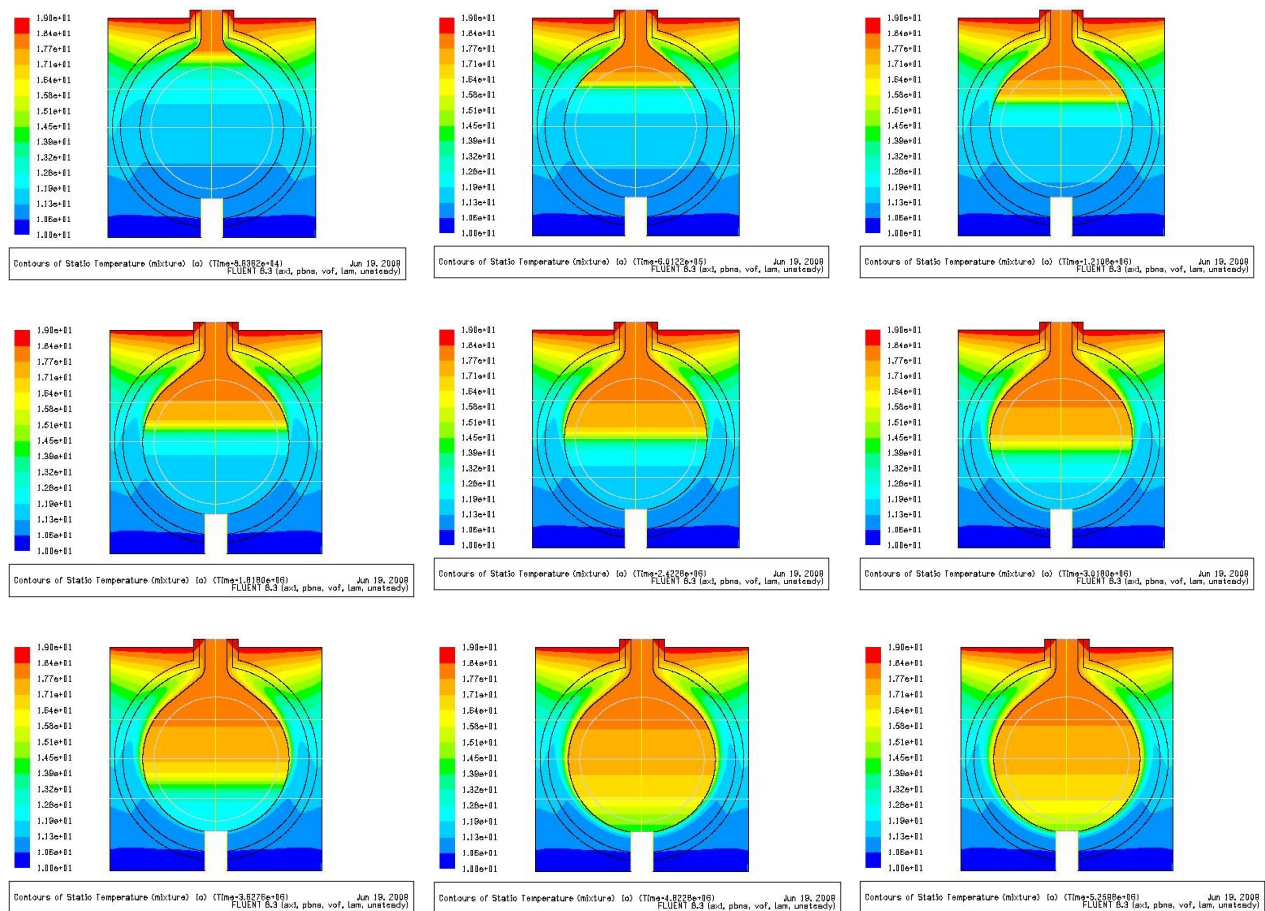


Figure 4-11. Montage of KamLAND CFD simulation temperature profile.

The montage in Figure 4-1 displays the CFD simulation after one day of purification. The newly purified LS has already traversed the chimney and is entering the spherical balloon. At this point, a clear interface is visible. Of concern is the high velocity magnitudes displayed in the chimney.

After a week of purification as seen in Figure 4-2, this slightly level interface between the old and new LS is present in both the CFD and  $^{222}\text{Rn}$  tracking. The maximum velocity magnitude has decreased by an order of  $10^3$  after the simulation has been running for an extended period of time. This behavior was observed in earlier simulations. The dark blue in

Figure 4-1 indicates velocities flow below  $10^{-5}$  meters per second which is within the range of observed values.

After two weeks of the multiphase purification CFD simulation displayed in Figure 4-3, the VOF contours contain a noticeable angle slope from the axis towards the outside. This is not seen the the  $^{222}\text{Rn}$  tracking, but this process has trouble seeing events that lie close along the surface of the balloon. It is a prediction that the purified LS has started to travel along the surface of the balloon as indication by the stream lines of the stream function contour plot.

In Figure 4-4, the VOF contours plot displays a swelling that runs along the axis of the model. It has been noted on observations of the purification process, that at this 3.5 meter mark, there is noticeable mixing and that the expected level stratification interface starts to disappear in the  $^{222}\text{Rn}$  model. In the top left figure, the purified LS appears to be strongly following along the circular path of the edge of the balloon. Again, in the VOF contour plot in Figure 4-5, there is not a level interface as predicted by the  $^{222}\text{Rn}$  tracking plot.

From the five week mark, displayed in Figure 4-6, to the end of the purification, displayed in Figure 4-9, it is interesting to note that in the plots of the  $^{222}\text{Rn}$  event tracking, the cluster of dots no longer follows the predicted line of volumetric filling and as time lapses, are noticeably absent from the bottom of the LS detector. This compelling case demonstrates that the  $^{222}\text{Rn}$  events are occurring less than what is expected because the flow is moving along the balloon in the detector during this purification process. There is clearly some kind of a mixing boundary occurring around 3.5 meters above the center that prevents the longitudinal movement of the purified LS along the z-axis and instead reroutes it towards the boundary of the balloon.

One complete volume (1 kton) of the liquid scintillator inside the balloon has been purified and replaced back into the balloon as shown in Figure 4-10. The majority of the measured  $^{222}\text{Rn}$  events are still in the upper region of the scintillator, while the region from 3.5 to -3.5 meters remained unpurified.

The spacial distribution plot shown Figure 4-12 provides some backup evidence that the swelling occurring in the CFD simulation phase contour plots are actual physical representations of the purification system. The plot was taken roughly between the sixth and seventh week of purification. Because the fiducial volume cut has been removed, this plot is a closer reference to the distribution of the purified LS with respect to radial coordinates. In the plot, there is a noticeable absence of events in the center of the detector; this absence is clearly visible in the CFD images, Figure 4-6 and Figure 4-7, that represent the estimated time of Figure 4-12.

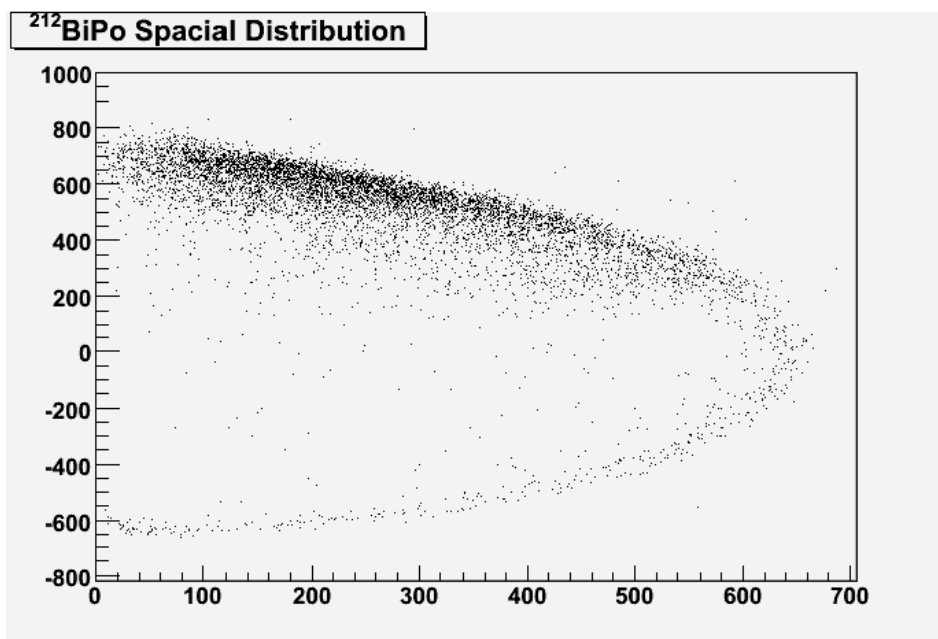


Figure 4-12. Spacial distribution of BiPo events with the fiducial volume cut removed.

## CHAPTER 5 CONCLUSIONS

Working on a complex computational fluid dynamics (CFD) simulation is a learning process of trial and error to determine what assumptions, physical models, and solution parameters are required to obtain an accurate representation of the problem being modeled. The modeling of the purification process of the KamLAND experiment posed a unique challenge in creating a CFD simulation to model the relatively small velocity magnitudes due to natural convection and the fluid interface between the purified and unpurified liquid scintillator (LS) in a large spherical domain over the time span of two months. Another challenge of the problem, because of physical constraints of the KamLAND experiment, the only empirical data concerning the flow and interaction between the purified and unpurified LS was from the method of tracking  $^{222}\text{Rn}$  daughters. The plots obtained from this method could not be compared directly to the CFD simulated plots of interaction between these fluids, but served more as a reference.

For the CFD simulation, the geometry and meshing of the model played important roles in the accuracy and converging of solutions of the model. Modifications were made to the geometry so that a 2D axisymmetric model could be applied to simplify the 3D geometry. Also, most of the thin walls, in comparison to the dimensions of the overall geometry, were modeled as edges with an assigned wall thickness for 1D conduction heat transfer calculations. These modifications helped greatly reduce the computational resources required. For the mesh of the model, boundary layers, consisting of highly dense rows of cells along a wall, were attached to edges in the domain to capture the details of the fluid flow at the walls. A high degree of resolution of the mesh in the fluid domain was determined to be required to be able to accurately

portray the effect of natural convection. Without this high resolution of the mesh, convergence of the solution of the simulation was unobtainable due to large mass continuity residuals.

When solving the CFD simulation using FLUENT, the following assumptions and physical models were used to represent the KamLAND experiment: 2D axisymmetric geometry, flow and energy equations coupled, Boussinesq approximation to model natural convection, and the volume of fraction (VOF) model to track the interface between the purified and unpurified LS. Also during the CFD simulation, the reductions of the under-relaxation factors of the variables, especially the momentum variable, of the governing equations were found to be important to the accuracies of the solutions of the simulation. Without these reductions, unrealistic or diverging solutions were encountered. With these assumptions and physical models, a CFD simulation of the two months of the KamLAND purification process was completed. At the beginning of the CFD simulation, it took approximately eight days to calculate thirty days of data, which is a ratio of 1:3.75. Towards the end of the simulation, when larger time steps were used, a ratio of 1:12 was found to be the typical. This meant that for every day of computing, roughly two weeks of the purification process was simulated.

The accuracy of the results obtained from the CFD simulation is somewhat questionable. Initially, for the first two weeks of the purification process simulated, a comparison of the similar results of the  $^{222}\text{Rn}$  events time-dated plots and the VOF contour time-date plots indicated the accuracy of the CFD simulation. But past this point of time, comparison of the two plots started differing. The FLUENT time-dated plots clearly indicated that the purified LS started to flow along the surface of the spherical balloon. This was also evident in the  $^{222}\text{Rn}$  time-dated plots, where the predicted stratification level deviated from the events detected around the origin mark of the z-axis. Instead of the events continuing downward in a horizontal layer along the z-axis,

past a horizontal interface at the origin, events were no longer detected in the middle of the domain, but along the balloon's surface. Though the main difference observed in the time-dated plots comparison was the sloping from the z-axis that occurred along the two liquid's interface in the FLUENT plot of the VOF contours. The top of the slope was approximately 3.5 meters above the origin along the z-axis and seemed to indicate a region of the unpurified LS that acted as a barrier that resisted the purified LS and redirected it outward. Another possible cause of this outward sloping that was suggested was the spherical shape of the balloon. There are not any previous studies to be found on the possible effects this shape has on the fluid flow within it. From discussions with the KamLAND Collaboration, it was noted that below this same positive elevation level of 3.5 meters above the origin there appeared to be a spherical region of fluid that the purified LS was not able to progress any further. This was not seen in the  $^{222}\text{Rn}$  events plots, but possibly evident in BiPo events plots with the fiducial volume cut removed. The BiPo events plot showed events densely clustered along the surface of the balloon and with an outward slope in the interface. From these discussions, it was assumed that the CFD simulation is accurate enough to serve as a representation of the purification process of the KamLAND experiment

The CFD simulation will be used to test proposed improvements to the purification process for future purification programs of KamLAND. The proposed improvements, with the aim of obtaining a horizontally stratified interface and minimizing natural convection, involve varying the physical properties, such as the density, and/or the temperature of the purified LS entering the detector. It is hoped that enough CFD simulations with these improvements can be completed before the next purification program to act as guides for the implementation of a more efficient purification process that will be able to meet the reduction goals necessary for the objectives of the KamLAND experiment.

## REFERENCES

- Anderson, J. D., Jr. (1995). *Computational fluid dynamics: the basics with applications*. New York: McGraw-Hill, Inc.
- ANSYS® FLUENT (Version 6.3). FLUENT 6.3 User's Guide [Software manual].
- Batchelor, G. K. (1967). *An introduction to fluid dynamics*. Cambridge, England: Cambridge University Press
- Bejan, A. (2004). *Convection heat transfer* (3rd ed.). New Jersey: John Wiley and Sons
- Campbell, C. E. (2002). Natural convection in a rectangular enclosure with a pipe attached. M.S. dissertation, University of Massachusetts Lowell, United States -- Massachusetts. Retrieved June 8, 2009, from Dissertations & Theses: Full Text database. (Publication No. AAT 1409915).
- Catton, I. (1978). Natural convection in enclosures. *Proceedings of the sixth international heat transfer conference, Toronto* (Vol. 6). Washington, D.C.: Hemisphere Publishing Corp.
- Ede, A. J. (1967). Advances in free convection. *Advances in heat transfer* (Vol. 4). New York: Academic Press
- Freitas, C. J. (Ed.). (1993). The CFD triathlon: Three laminar flow simulations by commercial CFD codes. Presented at the *Fluids Engineering Conference*, Washington, D.C. (FED-Vol. 160). New York: ASME, United Engineering Center
- Gebhart, B. (1979). Buoyancy induced fluid motions characteristic of applications in technology. *The 1978 Freeman Scholar Lecture, J. Fluid Engr* (Vol. 101).
- Hoogendorn, C. J. (1986). Natural convection in enclosures. *Proceedings of eighth international heat transfer conference, San Francisco* (Vol. 1). Washington, D.C.: Hemisphere Publishing Corp.
- Iwamoto, T. (2003). Measurement of reactor anti-neutrino disappearance in KamLAND. Ph.D. dissertation, Tohoku University, Japan. Retrieved June 6, 2009, from <http://kamland.lbl.gov/Dissertations/>

- Jing, X., Xiao, J., & Zhou, Z. (2005) Multi-dimensional simulation of hydrogen mixing and transport in the containment using CFD codes. Presented at the 18<sup>th</sup> international conference on structural mechanics in reactor technology, Beijing, China (SMiRT 18-P02-8). Retrieved February 5, 2009, from <https://www.iasmirt.org/iasmirt-2/SMiRT18/>
- Kamioka Liquid Scintillator Antineutrino Detector. (2009, May 19). In *Wikipedia, The Free Encyclopedia*. Retrieved May 19, 2009, from [http://en.wikipedia.org/w/index.php?title=Kamioka\\_Liquid\\_Scintillator\\_Antineutrino\\_Detector&oldid=290888735](http://en.wikipedia.org/w/index.php?title=Kamioka_Liquid_Scintillator_Antineutrino_Detector&oldid=290888735)
- KamLAND Collaboration (n.d.) Retrieved May 19, 2009, from <http://kamland.lbl.gov/>
- Kishimoto, Y. (2007). KamLAND status for solar neutrino phase. *J. Phys.: Conf. Ser.* 120. doi: 10.1088/1742-6596/120/5/052010
- Ostrach, S. (1964). Laminar flows with body forces: High speed aerodynamics and jet propulsion. In F. K. Moore (Ed.), *Theory of laminar flows* (Vol. 4). Princeton University Press
- Ostrach, S. (1972). Natural convection in enclosures. *Advances in heat transfer* (Vol. 8). New York: Academic Press
- Ostrach, S. (1982). Natural convection heat transfer in cavities and cells. *Proceedings of seventh international heat transfer conference, Munich* (Vol. 1). Washington, D.C.: Hemisphere Publishing Corp.
- O'Malley, C. (2003). Computational fluid dynamics model of natural convection airflow inside a commercial 30" wall oven using FLUENT. M.S.M.E. dissertation, University of Louisville, United States -- Kentucky. Retrieved June 8, 2009, from Dissertations & Theses: Full Text database. (Publication No. AAT 1459527).
- Stein, E., de Borst, R., Hughes, T. J. R. (Eds.). (2004). *Encyclopedia of Computational Mechanics* (Vol. 3: *Fluids*). West Sussex, England: John Wiley & Sons, Ltd.
- Suzuki, A. et al. (2005). Results from KamLAND reactor neutrino detection. *Phys. Scr.* T121, 33-38. doi: 10.1088/0031-8949/2005/T121/004
- Tajima, O. (2003). Measurement of electron anti-neutrino oscillation parameters with a large volume liquid scintillator detector, KamLAND. Phd. dissertation, Tohoku University, Japan. Retrieved June 6, 2009, from <http://kamland.lbl.gov/Dissertations/>
- Yao, H. (1999). Studies of natural convection in enclosures using the finite volume method. Ph.D. dissertation, York University (Canada), Canada. Retrieved June 6, 2009, from Dissertations & Theses: Full Text database. (Publication No. AAT NQ42781)
- Holman, J.P. (2002) *Heat transfer* (9th ed.). New York: McGraw-Hill

## APPENDIX A KAMLAND COLLABORATION

### **KamLAND collaboration**

K. Eguchi,<sup>1</sup> S. Enomoto,<sup>1</sup> K. Furuno,<sup>1</sup> J. Goldman,<sup>1</sup> H. Hanada,<sup>1</sup> H. Ikeda,<sup>1</sup> K. Ikeda,<sup>1</sup> K. Inoue,<sup>1</sup> K. Ishihara,<sup>1</sup> W. Itoh,<sup>1</sup> T. Iwamoto,<sup>1</sup> T. Kawaguchi,<sup>1</sup> T. Kawashima,<sup>1</sup> H. Kinoshita,<sup>1</sup> Y. Kishimoto,<sup>1</sup> M. Koga,<sup>1</sup> Y. Koseki,<sup>1</sup> T. Maeda,<sup>1</sup> T. Mitsui,<sup>1</sup> M. Motoki,<sup>1</sup> K. Nakajima,<sup>1</sup> M. Nakajima,<sup>1</sup> T. Nakajima,<sup>1</sup> H. Ogawa,<sup>1</sup> K. Owada,<sup>1</sup> T. Sakabe,<sup>1</sup> I. Shimizu,<sup>1</sup> J. Shirai,<sup>1</sup> F. Suekane,<sup>1</sup> A. Suzuki,<sup>1</sup> K. Tada,<sup>1</sup> O. Tajima,<sup>1</sup> T. Takayama,<sup>1</sup> K. Tamae,<sup>1</sup> H. Watanabe,<sup>1</sup> J. Busenitz,<sup>2</sup> Z. Djurcic,<sup>2</sup> K. McKinny,<sup>2</sup> D-M. Mei,<sup>2</sup> A. Piepke,<sup>2</sup> E. Yakushev,<sup>2</sup> B.E. Berger,<sup>3</sup> Y.D. Chan,<sup>3</sup> M.P. Decowski,<sup>3</sup> D.A. Dwyer,<sup>3</sup> S.J. Freedman,<sup>3</sup> Y. Fu,<sup>3</sup> B.K. Fujikawa,<sup>3</sup> K.M. Heeger,<sup>3</sup> K.T. Lesko,<sup>3</sup> K.-B. Luk,<sup>3</sup> H. Murayama,<sup>3</sup> D.R. Nygren,<sup>3</sup> C.E. Okada,<sup>3</sup> A.W. Poon,<sup>3</sup> H.M. Steiner,<sup>3</sup> L.A. Winslow,<sup>3</sup> G.A. Horton-Smith,<sup>4</sup> R.D. McKeown,<sup>4</sup> J. Ritter,<sup>4</sup> B. Tipton,<sup>4</sup> P. Vogel,<sup>4</sup> C.E. Lane,<sup>5</sup> T. Miletic,<sup>5</sup> P. Gorham,<sup>6</sup> G. Guillian,<sup>6</sup> J. Learned,<sup>6</sup> J. Maricic,<sup>6</sup> S. Matsuno,<sup>6</sup> S. Pakvasa,<sup>6</sup> S. Dazeley,<sup>7</sup> S. Hatakeyama,<sup>7</sup> M. Murakami,<sup>7</sup> R.C. Svoboda,<sup>7</sup> B.D. Dieterle,<sup>8</sup> M. DiMauro,<sup>8</sup> J. Detwiler,<sup>9</sup> G. Gratta,<sup>9</sup> K. Ishii,<sup>9</sup> N. Tolich,<sup>9</sup> Y. Uchida,<sup>9</sup> M. Batygov,<sup>10</sup> W. Bugg,<sup>10</sup> H. Cohn,<sup>10</sup> Y. Efremenko,<sup>10</sup> Y. Kamyshev,<sup>10</sup> A. Kozlov,<sup>10</sup> Y. Nakamura,<sup>10</sup> C.R. Gould,<sup>11</sup> H.J. Karwowski,<sup>11</sup> D.H. Markoff,<sup>11</sup> J.A. Messimore,<sup>11</sup> K. Nakamura,<sup>11</sup> R.M. Rohm,<sup>11</sup> W. Tornow,<sup>11</sup> A.R. Young,<sup>11</sup> and Y-F. Wang<sup>12</sup>

<sup>1</sup> Research Center for Neutrino Science, Tohoku University, Sendai 980-8578, Japan

<sup>2</sup> Department of Physics and Astronomy, University of Alabama, Alabama 35487, USA

<sup>3</sup> Physics Department, University of California at Berkeley and Lawrence Berkeley National Laboratory, Berkeley, California 94720, USA

<sup>4</sup> W. K. Kellogg Radiation Laboratory, California Institute of Technology, Pasadena, California 91125, USA

<sup>5</sup> Physics Department, Drexel University, Philadelphia, Pennsylvania 19104, USA

<sup>6</sup> Department of Physics and Astronomy, University of Hawaii at Manoa, Honolulu, Hawaii 96822, USA

<sup>7</sup> Department of Physics and Astronomy, Louisiana State University, Louisiana 70803, USA

<sup>8</sup> Physics Department, University of New Mexico, Albuquerque New Mexico 87131, USA

<sup>9</sup> Physics Department, Stanford University, California 94305, USA

<sup>10</sup> Physics Department, University of Tennessee, Tennessee 37996, USA

<sup>11</sup> Triangle Universities Nuclear Laboratory, Durham, NC 27708, USA and

Physics Departments at Duke University, North Carolina State University, and the University of North Carolina at Chapel Hill

<sup>12</sup> Institute of High Energy Physics, Beijing 100039, People's Republic of China

## APPENDIX B METHOD OF TRACKING $^{222}\text{Rn}$ DAUGHTERS

*Note: This explanation of the tracking of  $^{222}\text{Rn}$  daughters to determine the location of purified LS was provided by Chris Grant, a member of the Physics Department of the University of Alabama, which is a part of the KamLAND Collaboration.*

The gaseous  $^{222}\text{Rn}$  isotope appears naturally within our atmosphere and acts as a radioactive background in KamLAND (it eventually decays into  $^{210}\text{Pb}$  which has ~22 year half life;  $^{210}\text{Pb}$  will then decay into  $^{210}\text{Bi}$  and  $^{210}\text{Po}$ , both of which will hide the solar neutrino signal we want to observe).  $^{222}\text{Rn}$  can enter KamLAND scintillator through tiny leaks in the pipes which carry the purified scintillator from the distillation system back into the detector.

Extensive leak testing is conducted to minimize the amount of  $^{222}\text{Rn}$  that sneaks into the purified scintillator, but there is always a tiny amount that gets into the detector. As long as the amount of  $^{222}\text{Rn}$  that sneaks into the purified scintillator is less than 1 mBq in activity, our purification will not be ruined. (Note: 1 Bq = 1 decay/second, and 1 mBq = 1 decay/1000 seconds; Bq means “Bequerel”). The amount of  $^{222}\text{Rn}$  entering the detector is monitored as it is being filled during purification to make sure there is not recontamination the scintillator.

KamLAND is an extremely sensitive particle detector, so observing only a few atoms of  $^{222}\text{Rn}$  in the 1-kton detector is possible (the time, position and energy of all events in the detector are collected). Monitoring  $^{222}\text{Rn}$  contamination also provides a picture of the separation between purified and un-purified scintillator.  $^{222}\text{Rn}$  has a 3.8 day half life, so it will have already

decayed away completely in the un-purified scintillator. It will be observable in the purified scintillator for roughly 1 month before it has completely decayed away. To measure  $^{222}\text{Rn}$ , the decay scheme is shown below in Figure B-1.

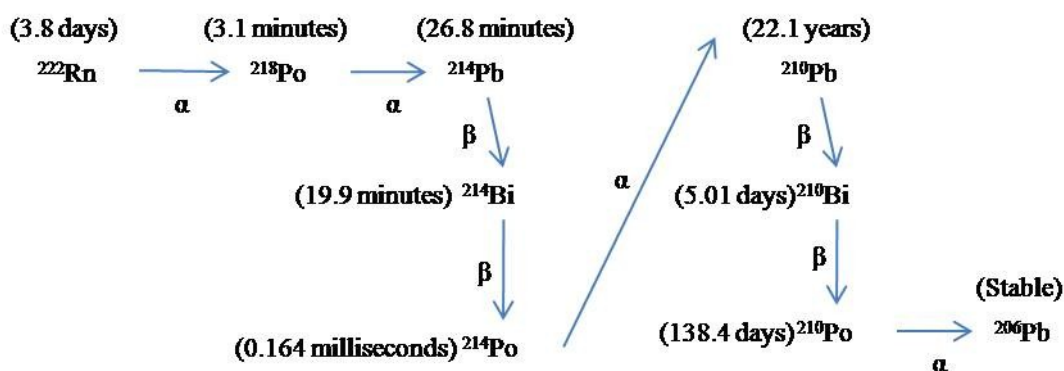


Figure B-1. Decay scheme for  $^{222}\text{Rn}$ .

The half-lives are shown in brackets and the decay type is given next to the arrows. We can measure  $^{222}\text{Rn}$  by measuring the activity of its daughters,  $^{214}\text{Bi}$  and  $^{214}\text{Po}$ .  $^{210}\text{Pb}$  will feed  $^{210}\text{Bi}$  and  $^{210}\text{Po}$  for a long time, which is bad for KamLAND. All the daughters after  $^{222}\text{Rn}$  (but before  $^{210}\text{Pb}$ ) have very short half-lives compared to 3.8 day half-life of  $^{222}\text{Rn}$ . This means that the daughters,  $^{214}\text{Bi}$  and  $^{214}\text{Po}$ , will have the same activity as  $^{222}\text{Rn}$  (this is known as secular equilibrium).

Why use  $^{214}\text{Bi}$  and  $^{214}\text{Po}$ ? It can be seen that if a  $^{214}\text{Bi}$  atom decays into  $^{214}\text{Po}$ , the  $^{214}\text{Po}$  will decay, on average, within 0.164 milliseconds (very fast!). It is highly improbable that any other events will occur in such a short time window after a  $^{214}\text{Bi}$  decay. This means we can look at all the physics events in the KamLAND data and only choose events that “coincide” with this very fast decay of  $^{214}\text{Po}$  after  $^{214}\text{Bi}$ .

To choose  $^{214}\text{Bi}$  events, an energy selection cut is made in the data (since  $^{214}\text{Bi}$  decays with a certain energy that follows a known statistical distribution):  $-0.45 < E_{\text{prompt}} < 3.00$  MeV

( $^{214}\text{Bi}$  is the “prompt” event). A time window is opened in the data ( $\sim 1.2$  milliseconds) after this “prompt”  $^{214}\text{Bi}$  event and the possible  $^{214}\text{Po}$  events are collected using another energy selection cut:  $-0.45 < E_{\text{delay}} < 0.80$  MeV ( $^{214}\text{Po}$  is the “delay” event). Event pairs are also required to be no more than 120 cm apart from one another. Pairs of events that satisfy the conditions above are collected. Histograms of the data can be seen below in Figure B-2.

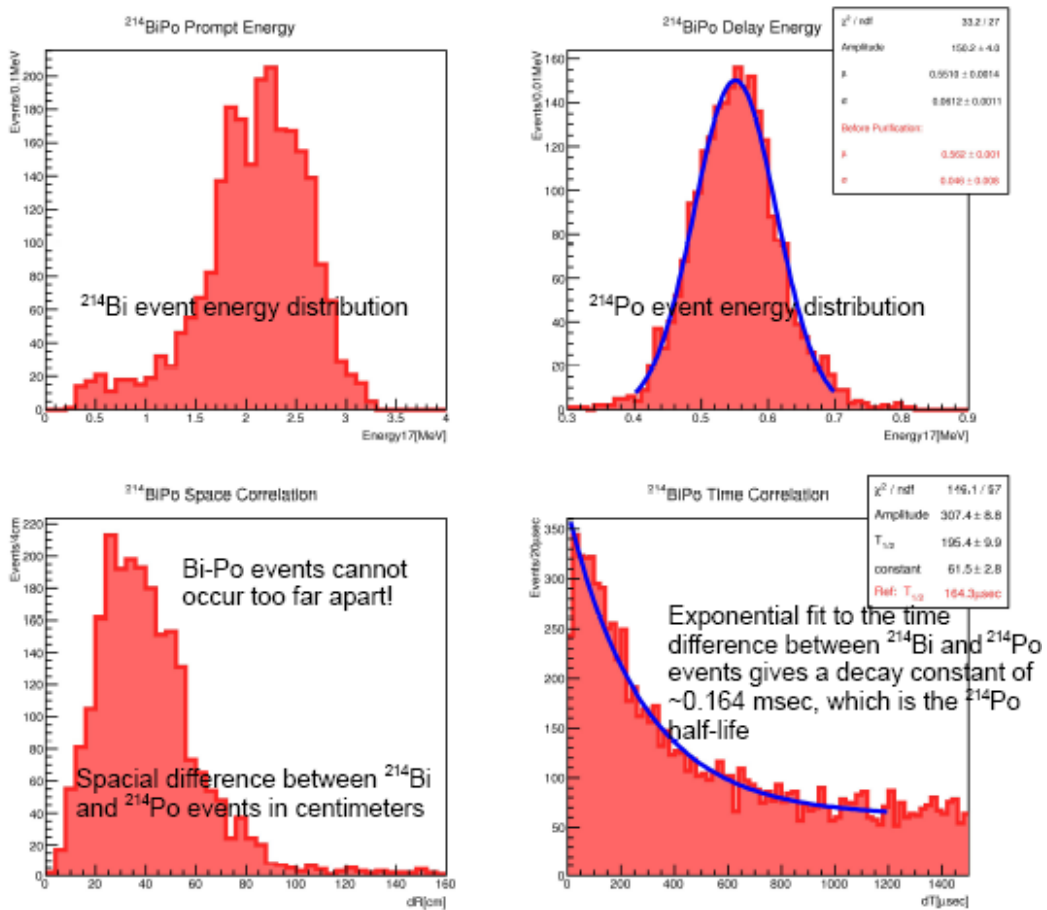


Figure B-2. Pairs of events that satisfy energy selection cut for  $^{214}\text{Bi}$ - $^{214}\text{Po}$  events.

Monte Carlo simulations of  $^{214}\text{Bi}$ - $^{214}\text{Po}$  events in the KamLAND detector agree very well with the data shown in Figure B-2, confirming the event selection. Each one of these  $^{214}\text{Bi}$ - $^{214}\text{Po}$  pair

of events in the data set corresponds to a single  $^{222}\text{Rn}$  decay. Counting the number of  $^{214}\text{Bi}$ - $^{214}\text{Po}$  pairs over a period of time will tell us the  $^{222}\text{Rn}$  activity (number of decays per second). This can then be used to plot the position of these pairs of events in the detector as shown in Figure B-3.

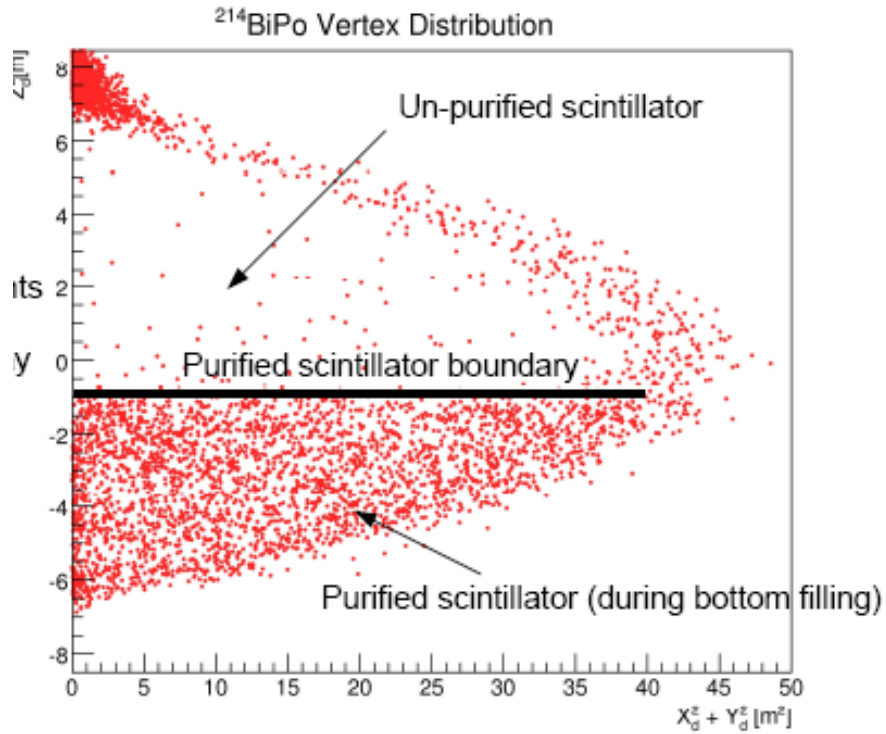


Figure B-3. Dots representing  $^{214}\text{Bi}$ - $^{214}\text{Po}$  event pair from the decay of  $^{222}\text{Rn}$  in the detector.

## APPENDIX C MATERIALS PARAMETERS

- Liquid Scintillator @ 15 °C
  - Density  $\rho = 777.54 \text{ kg/m}^3$  (Iwamoto 2003)
  - Specific Heat  $C_p = 2,172 \text{ J/kg}\cdot\text{K}$  (J. Chem. Phys. 122, 084907 (2005))
  - Thermal Conductivity  $k = 0.13829 \text{ W/m}\cdot\text{K}$
  - Dynamic Viscosity  $\mu = 14.8 \times 10^{-4} \text{ kg/m}\cdot\text{s}$  (Mitsui)
  - Thermal Expansion  $\beta = 9.53 \times 10^{-4} \text{ 1/K}$
  - Molecular Weight  $MW \sim 91.6$
  
- Buffer Oil @ 15 °C
  - Density  $\rho = 777.32 \text{ kg/m}^3$  (Tajima 2003)
  - Specific Heat  $C_p = 2,172 \text{ J/kg}\cdot\text{K}$  (J. Chem. Phys. 122, 084907 (2005))
  - Thermal Conductivity  $k = 0.13829 \text{ W/m}\cdot\text{K}$
  - Dynamic Viscosity  $\mu = 12.9 \times 10^{-4} \text{ kg/m}\cdot\text{s}$  (Mitsui)
  - Thermal Expansion  $\beta = 8.99 \times 10^{-4} \text{ 1/K}$
  - Molecular Weight  $MW \sim 109.5$
  
- Engine Oil, Unused @ 20 °C (Holman 2002)
  - Density  $\rho = 888.23 \text{ kg/m}^3$
  - Specific Heat  $C_p = 1,880 \text{ J/kg}\cdot\text{K}$
  - Thermal Conductivity  $k = 0.145 \text{ W/m}\cdot\text{K}$
  - Dynamic Viscosity  $\mu = 0.7994 \text{ kg/m}\cdot\text{s}$
  - Thermal Expansion  $\beta = 7.0 \times 10^{-4} \text{ 1/K}$
  
- Anti Water @ 15 °C (Holman 2002)
  - Density  $\rho = 999.1 \text{ kg/m}^3$
  - Specific Heat  $C_p = 4,186 \text{ J/kg}\cdot\text{K}$
  - Thermal Conductivity  $k = 0.595 \text{ W/m}\cdot\text{K}$
  - Dynamic Viscosity  $\mu = 11.2 \times 10^{-4} \text{ kg/m}\cdot\text{s}$
  - Thermal Expansion  $\beta = 1.51 \times 10^{-4} \text{ 1/K}$
  
- Nylon (Holman 2002)
  - Density  $\rho = 1,150 \text{ kg/m}^3$
  - Specific Heat  $C_p = 1,700 \text{ J/kg}\cdot\text{K}$
  - Thermal Conductivity  $k = 0.25 \text{ W/m}\cdot\text{K}$

- Plexiglass (Holman 2002)
  - Density  $\rho = 1,200 \text{ kg/m}^3$
  - Specific Heat  $C_p = 1,500 \text{ J/kg}\cdot\text{K}$
  - Thermal Conductivity  $k = 0.2 \text{ W/m}\cdot\text{K}$

## APPENDIX D BOUNDARY CONDITIONS

- Antiwater\_Bottom : Wall
  - Temperature = 10 °C
  - Wall Thickness = 0.016 m
  - Material = Steel
- Antiwater\_Cylinder : Wall
  - Temperature = UDF Temp\_Profile
  - Wall Thickness = 0.016 m
  - Material = Steel
- Balloon : Wall
  - Coupled
  - Wall Thickness = 0.000135 m
  - Material = Nylon
- Dome / Top : Wall
  - Convection
  - HT Coeff = 5 W/m<sup>2</sup>·K
  - Temp<sub>FS</sub> = 19 °C
  - Wall Thickness = 0.016 m
  - Material = Steel
- Inlet : Mass Flow Inlet
  - Temperature = 17 °C
  - Mass Flow = 0.238 kg/s
  - Velocity = 9.7 x 10<sup>-5</sup> m/s
- Inner\_BufferOil : Wall
  - Coupled
  - Wall Thickness = 0.003 m
  - Material = Plexiglass
- Outer\_BufferOil : Wall
  - Coupled
  - Wall Thickness = 0.016 m
  - Heat Generat. = 7.48 W/m<sup>3</sup>
  - Material = Steel\
- Outlet : Mass Flow Inlet (Axial Component = -1)
  - Temperature = 11 °C
  - Mass Flow = 0.238 kg/s
  - Velocity = 9.7 x 10<sup>-5</sup> m/s

## APPENDIX E USER DEFINED FUNCTION TEMPERATURE PROFILE

### UDF Temperature Profile

```
/****** */
/* */
/* temp_profile.c */
/* UDF for specifying 4th order polynomial */
/* temperature profile on a boundary wall */
/* */
/****** */

#include "udf.h"

DEFINE_PROFILE(temp_profile, thread, position)
{
    real r[ND_ND];
    real x;
    face_t f;

    begin_f_loop(f, thread)
    {
        F_CENTROID(r, f, thread);
        x = r[0];
        F_PROFILE(f, thread, position) = 0.0003 * x^4 + 0.0027 * x^3 - 0.0015 *
x^2 + 0.1381 * x + 285.15;
    }
    end_f_loop(f, thread)
}
```

## APPENDIX F KAMLAND CFD WORK SHEET

*Table F-1. KamLAND\_2Dv10 Work Sheet.*

Data File Name	Steady	Unsteady	Explicit	Implicit	Flow	Volume Fraction	Energy	SIMP LE	SIMP LEC	P50	Pressure	Density	Body Forces	Mom.	Volume Fraction	Energy	Pressure	Momentum	Volume Fraction	Energy	Iterations	Time Step	No. of Time Steps	Result	Plan	
0000000-0000	X		X			X		X			0.30	1	1	0.70	N/A	1	BFW	1st	mHRIC	2nd	2	N/A	N/A	Temperature Profile Obtained	Perform transient solution	
0000744-0180		X	X		X	X	X	X			0.15	1	1	0.15	N/A	0.8	BFW	1st	mHRIC	2nd		10s		Slight Thermal Mixing	Reduce Energy URF	
0043200-4431		X	X		X	X	X	X			0.15	1	0.5	0.15	0.2	1	BFW	1st	mHRIC	2nd		20s			Increase Time Step	
0075561-5580		X		X	X	X	X	X			0.20	1	0.5	0.05	0.2	1	BFW	1st	mHRIC	2nd		40s		No Problem	Increase Time Step	
0086362-7020		X		X	X	X	X	X			0.20	1	0.5	0.05	0.2	1	BFW	1st	mHRIC	2nd		80s		No Problem	Increase Time Step	
439260-17280		X		X	X	X	X	X			0.20	1	0.5	0.05	0.2	1	BFW	1st	mHRIC	2nd		120s				
213220-30720		X		X	X	X	X	X			0.20	1	0.5	0.05	0.2	1	BFW	1st	mHRIC	2nd		120s				
Current		X		X	X	X	X	X			0.20	1	0.5	0.05	0.2	1	BFW	1st	mHRIC	2nd		120s				
<i>Note: For all cases, the case is Axisymmetric, Energy, VOF, Bous. Eq.</i>																										